Monthly Notices of the ROYAL ASTRONOMICAL SOCIETY

MNRAS **507,** 3312–3330 (2021) https://doi.org/10.1093/mnras/stab2297
Advance Access publication 2021 August 10

STEP survey – II. Structural analysis of 170 star clusters in the SMC

M. Gatto [1,2★] V. Ripepi [1] M. Bellazzini [3] M. Tosi,[3] M. Cignoni [3,4,5] C. Tortora [1] S. Leccia,[1] G. Clementini,[3] E. K. Grebel,[6] G. Longo,[2] M. Marconi [1] and I. Musella [1]

[1]*INAF – Osservatorio Astronomico di Capodimonte, Via Moiariello 16, I-80131 Naples, Italy*
[2]*Department of Physics, University of Naples Federico II, C.U. Monte Sant'Angelo, Via Cinthia, I-80126 Naples, Italy*
[3]*INAF – Osservatorio di Astrofisica e Scienza dello Spazio, Via Gobetti 93/3, I-40129 Bologna, Italy*
[4]*Physics Department, University of Pisa, Largo Bruno Pontecorvo 3, I-56127 Pisa, Italy*
[5]*INFN, Largo Bruno Pontecorvo 3, I-56127 Pisa, Italy*
[6]*Astronomisches Rechen-Institut, Zentrum für Astronomie der Universität Heidelberg, Mönchhofstr 12-14, D-69120 Heidelberg, Germany*

Accepted 2021 July 28. Received 2021 July 27; in original form 2021 May 13

ABSTRACT

We derived surface brightness profiles in the *g* band for 170 Small Magellanic Cloud (SMC) star clusters (SCs) mainly located in the central region of the galaxy. We provide a set of homogeneous structural parameters obtained by fitting Elson–Fall–Freeman and King models. Through a careful analysis of their colour–magnitude diagrams we also supply the ages for a subsample of 134 SCs. For the first time, such a large sample of SCs in the SMC is homogeneously characterized in terms of their sizes, luminosities, and masses, widening the probed region of the parameter space, down to hundreds of solar masses. We used these data to explore the evolution of the SC's structural parameters with time. In particular, we confirm the existence of a physical mechanism that induces an increase of the core radius after 0.3–1.0 Gyr. We suggest that cluster mass could be the main parameter driving the inner expansion, as none of the SCs having $\log(M/M_{\odot}) \leq 3.5$ dex analysed in this work undergoes to such an expansion. We also detected a mass–size relationship almost over the entire range of SCs masses investigated here. Finally, our data suggest that globally the SMC SC system is dynamically evolved.

Key words: surveys – Hertzsprung-Russell and colour-magnitude diagrams – galaxies: star clusters: general – Magellanic Clouds.

1 INTRODUCTION

The Magellanic Clouds (MCs) are an excellent benchmark for the study of the evolution of star clusters (SCs). Their cluster system includes also very massive ($\log(M/M_{\odot}) \sim 5$ dex) SCs of young ($t \leq 1$ Gyr) or intermediate age ($1 \leq t \leq 7$ Gyr), which are absent in our Galaxy, enabling us to probe a broader region of the parameter space, and in turn, making it possible to investigate the evolutionary processes working in a cluster over cosmic time. Thanks to several studies aimed at the analysis of clusters in the Large Magellanic Cloud (LMC) and Small Magellanic Cloud (SMC), key progress in this field has been achieved in the last decades. Elson, Freeman & Lauer (1989) found a trend between the core radius r_c (the distance from the cluster centre where the surface brightness (SB) drops down to half its central value) and the age of clusters, namely, the older the SC, the larger the spread in core radius. This relationship was confirmed by subsequent works in the LMC (e.g. Elson 1991, 1992; Mackey & Gilmore 2003a; Carvalho et al. 2008), SMC (e.g. Mackey & Gilmore 2003b; Carvalho et al. 2008), and in other systems like M33, M51, M83, NGC 628, and NGC 1313 (e.g. Bastian et al. 2012; San Roman et al. 2012; Ryon et al. 2015, 2017; Chandar et al. 2016). Mackey & Gilmore (2003a) explored the possibility that some bias due to selection effects could explain this trend, but they ruled it out, concluding that the apparent behaviour reflects a real evolutionary process. In this scenario, all SCs formed with small core radii (∼2–3 pc), then some of them remained compact, while others, after hundreds of Myr, expanded their inner regions. However, the physical mechanism inducing the core expansion is still debated. Energy transfer from the inner to outer regions due to stellar mass black holes (BHs; Merritt et al. 2004; Mackey et al. 2007, 2008), mass loss due to stellar evolution (Mackey et al. 2007, 2008), and/or residual gas expulsion (Kroupa, Aarseth & Hurley 2001; Goodwin & Bastian 2006; Baumgardt & Kroupa 2007; Banerjee & Kroupa 2017) are the main processes invoked to explain the phenomenon. Also the presence of a central intermediate-mass black hole (IMBH) can lead to a core expansion (Baumgardt, Makino & Ebisuzaki 2004a,b). More likely, a combination of two or three of the above processes could provide the observed evolution in the core radius (e.g. Bastian et al. 2008).

A key ingredient for the study of the dynamical evolution of SCs is the availability of accurate and homogeneously derived surface brightness profiles (SBPs), extending as far as possible from the cluster centre. Here we focus on the SMC, which contains a large sample of SCs. The most complete and recent catalogue by Bica et al. (2020) reports about 850 SMC objects classified as SCs. Nowadays, thanks to many surveys covering both the MCs [e.g. Magellanic Clouds Photometric Survey (MCPS), Survey of the MAgellanic Stellar History (SMASH), SMC in Time: Evolution of a Prototype

★ E-mail: massimiliano.gatto@inaf.it

interacting late-type dwarf galaxy (STEP), Yes, Magellanic Clouds Again (YMCA), VIsible Soar photometry of star Clusters in tApii and Coxi HuguA (VISCACHA); Zaritsky, Harris & Thompson 1997; Ripepi et al. 2014; Nidever et al. 2017; Maia et al. 2019], it is feasible to collect detailed SBPs for a statistically significant sample of SCs to better understand the mechanisms ruling SC evolution. King profiles are employed to approximate SBP shapes of most of the Galactic globular clusters (GGC; e.g. King 1962). However, Elson, Fall & Freeman (1987) pointed out that a different kind of analytical function, nowadays called Elson–Fall–Freeman (EFF) profile, better describes the SBP of the LMC SCs. The main difference between the two quoted profiles is that the latter does not present a 'truncation' at large radii that separates the SC from the field. Which of the two profiles better assesses the SBP shape of the MCs SCs is still debated. Hill & Zaritsky (2006, hereafter HZ06) and later Werchan & Zaritsky (2011) analysed structural parameters of 204 SMC and 1066 LMC SCs, respectively, fitting the SBP with both the above-mentioned profiles. Despite the significant statistical sample of analysed SCs these authors did not find any favoured profile, both of them were satisfactory for the majority of the SCs, with King profiles performing slightly better. Very recently, Santos et al. (2020) carried out a detailed analysis of 83 SCs located at the periphery of both the MCs in the context of the VISCACHA (Maia et al. 2019) survey, with the SOuthern Astrophysical Research (SOAR) telescope. The analysis of the SBPs of these 83 SCs, fitted with both King and EFF profiles, allowed these authors to confirm that the SPBs can be matched almost equally well by both EFF and King models. At the same time, they assessed the presence of an evolution of r_c for older SCs in both the LMC and SMC, as already suggested in the literature (Santos et al. 2020).

In this paper, we infer the dynamical evolution of a sample of SCs through an extensive work based on an accurate assessment of the SC main properties by means of the study of their SBPs in the *g* band and colour–magnitude diagrams (CMDs) in the *g* and *i* bands. Our aim is to provide the scientific community with new accurate structural parameters like sizes, luminosities, and masses derived via a model fitting of both King and EFF profiles. We also supply age estimates for a subsample of SCs. Our sample consists of 170 SMC SCs, whose photometry was obtained with the *'the SMC in Time: Evolution of a Prototype interacting late-type dwarf galaxy'* (STEP: PI: V. Ripepi; Ripepi et al. 2014) survey, which are already listed in the catalogue by Bica et al. (2020), located throughout the inner parts (most of them reside within $\sim 2^\circ$–3°) of the SMC, and spanning a wide range of ages and masses. Of these 170 SCs, 62 have never been examined before. Our sample extends the range of masses towards values lower than those already present in the literature. As far as we are aware, it is the first time that a wide range of structural parameters, from sizes to masses, have been derived homogeneously in the SMC. Moreover, these features are used to study the dynamical phase of SCs, probing the age of the SMC SC system, from the dynamical point of view. Finally, SC properties are also used as a tool to gain hints on the SMC environment by inspecting how they depend on the distance from the SMC centre. We exploit the data from the photometric STEP survey. This survey reaches $g \sim 25$ mag (in non-heavily crowded regions), well below the main-sequence turn-off (TO) of the oldest stellar population, allowing us to investigate accurately even SCs with very low SB. The high resolution of STEP even at faint magnitudes makes it feasible to achieve a reliable accuracy even for SCs of ~ 100 $M_\odot$, probing in detail a locus of the parameter space barely explored with a conspicuous number of SCs.

The paper is structured as follows. We present the observations and data reduction strategy along with the construction of the sample in Section 2. In Section 3, we describe the procedure adopted to derive the SBPs, while Section 4 presents the derivation of SC structural parameters. We report the age and mass assessment in Section 5. In Section 6, we present the main results of this work, while in Section 7 we discuss them. Finally, a brief summary is reported in Section 8.

2 DATA

2.1 The STEP survey

As mentioned above, the data used in this work were obtained in the context of the STEP survey, carried out with the VLT Survey Telescope (VST) as part of the Guaranteed Time Observations (GTO) awarded by the European Southern Observatory (ESO) to the Istituto Nazionale di Astrofisica (INAF). The telescope is equipped with OmegaCAM, a mosaic camera of 32-CCD, 16k × 16k detectors with a pixel scale of 0.214 arcsec pixel^{-1} and with a field of view (FOV) of 1 deg^2. STEP extends over 53 deg^2 covering the SMC and the Bridge connecting the two Clouds. Full details of the observing strategy can be found in Ripepi et al. (2014). That paper also presents a full description of the data reduction, including procedures of pre-reduction, astrometry, and stacking of the different dithered frames into a single mosaic image, which were performed with the VST–TUBE imaging pipeline (Grado et al. 2012). The point spread function (PSF) photometry was carried out using DAOPHOT IV/ALLSTAR(Stetson 1987, 1992). As for the photometric calibration, it was improved with respect to Ripepi et al. (2014), with the adoption of the local standard stars made available by the AAVSO Photometric All-Sky Survey (APASS). The different steps of the photometric calibration are sketched in Gatto et al. (2020), whereas full details will be provided elsewhere (Ripepi et al., in preparation). Here we only recall that the overall accuracy of the photometry is ∼0.02 and ∼0.025 mag in *g* and *i* bands, respectively. Finally, the photometrically calibrated catalogues were cleaned from extended/spurious objects by keeping only objects with typically $-0.6 \leq$ sharpness ≤ 0.7, where sharpness is an output parameter of the DAOPHOT package adopted to identify extended objects.

2.2 Building the star cluster sample

To achieve our goals, we built a statistically significant sample of SCs, covering as much as possible different regions of the SMC. We focused our research on all objects classified as SCs (i.e. those indicated with the letter C in the column Type of the catalogue) by Bica et al. (2008). Then, we restricted the list to those SCs whose spatial positions overlapped with tiles 3_3, 3_4, 3_5, 3_6, 3_7, 3_8, 4_4, 4_5, 4_6, 5_5, and 5_6 (see fig. 2 and table 2 in Ripepi et al. 2014, for the definition of the tiles).

Despite our efforts, we could not analyse all the 404 SCs present in Bica et al.'s (2008) catalogue and falling on the above quoted tiles. In fact, we had to discard almost all the SCs with a minor axis smaller than ∼0.5 arcmin, corresponding to about 40 per cent of the starting list, because they showed too noisy SBPs. Moreover, we had to reject also those SCs whose centres were too close to the edges of the tile (∼10 per cent) or which on the images did not appear as real SCs (∼10 per cent). At the end, we were left with 170 usable SCs. Fig. 1 shows the SC relative positions with respect to the SMC centre defined by classical Cepheids variables: $(\alpha_0, \delta_0) = (12.54, -73.11)$ (Ripepi et al. 2017). This centre is very similar to the one adopted by Gonidakis et al. (2009) based on K and M giants, i.e. $(\alpha_0, \delta_0) = (12.75, -73.10)$.

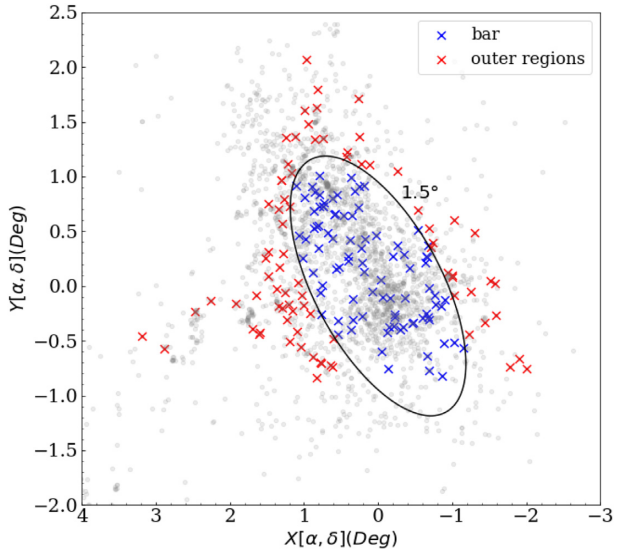

Figure 1. Positions of all 170 SCs studied in this paper, in a zenithal equidistant projection, with respect to the SMC centre (Ripepi et al. 2017). Small grey dots show the whole SC catalogue by Bica et al. (2020). Blue crosses represent SCs within an ellipse with its semimajor axis $a = 1.^{\circ}5$ and ellipticity $e = 0.5$, whereas red crosses are the SCs outside the ellipse (see Appendix B).

3 METHOD

For each SC we derived the SBP (i.e. mag arcsec^{-2} as a function of the clustercentric distance) by means of integrated aperture photometry. After a careful analysis of SPBs in both the *g* and *i* bands, we choose to work with the *g* band, since the data in this filter provide significantly less noisy SPBs for the large majority of the SCs in our sample. Detection of individual stars in such distant and crowded clusters is biased by significant incompleteness, with strong variation with distance from the cluster centre. Integrated photometry overcomes this problem, allowing a safe tracing of the light density distribution.

3.1 Star cluster centre estimation

The key to compute accurately the SBP of a SC is to carefully determine its centre. Our sample contains many SCs that are very patchy and irregular, making the centre estimation procedure rather tricky. Since the majority is also asymmetric, it is unsuitable to make use of algorithms, such as the mirror-autocorrelation method described by Djorgovski (1988), which takes advantage of the symmetry to properly determine the centre of an object (Mackey & Gilmore 2003a). Therefore, we preferred to use individual star positions to locate the 'centroid' of the cluster and define it as SC centre. To this aim, we employed an iterated two-dimensional kernel density estimation (KDE)[1] by using the star coordinates RA and Dec. as inputs to find the SC centre. As a starting point, we used the SC centres and major axes by Bica et al. (2020) to build surface density maps via KDE, obtained by calculating its value in a circular region centred on the SC with a radius twice its major axis. For each SC, we updated the SC centre by assigning it the coordinates where the surface density map has its maximum, and we repeated the same procedure until two successive estimated centres differ by less than 1 arcsec. To better assess the SC centre, we ran the KDE many times by varying the bandwidth[2] of the kernel function in the range 0.01–0.4 arcmin. Finally, we took the mean of all centroids as our best estimate for each SC centre.

To check the validity of our procedure, we compared our SC centres with those derived by Carvalho et al. (2008), who have 19 SCs in common with our sample. The mean difference between the two centre evaluations is below 2 arcsec. In the second and third column of Table C1 we listed all SC centres determined with the described procedure.

3.2 Surface brightness determination

We followed the procedure developed by Djorgovski (1988), which consists of dividing the entire annulus in eight sectors of equal area and evaluating the flux in each of them. The flux in each annulus was obtained through the open source PHOTUTILS package (Bradley et al. 2019), written in PYTHON. The SB of an annulus is then the median of the eight fluxes, and we adopted $\Delta_{\mu} = 1.4826 \times \mathrm{MAD}$, where MAD is the median absolute deviation, as their estimated uncertainty. This technique mitigates the impact of very bright or foreground stars on the SBP. Indeed, bright stars will increase the SB, and might generate artificial bumps in its shape, leading to wrong physical interpretations. This effect could be dramatic in our selected sample of SCs, since many of them have a low SB. The median ensures that sectors with such stars do not dominate the budget of the estimated SB.

In order to evenly sample inner and outer regions, many authors (e.g. Mackey & Gilmore 2003a,b; Carvalho et al. 2008) utilized four sets of annuli of different thickness. Since many SCs in our sample have a SB only marginally above the background level, in order to better assess the SB value at a given radius we preferred to deal with 16 sets of annuli, having widths between 1.0 and 4.0 arcsec with a step size of 0.2 arcsec. Since smaller annuli aim to sample the inner regions, we used those with sizes between 1.0–1.5 and 1.5–2.0 arcsec up to 20 and 30 arcsec from the centre, respectively. The remaining sets of annuli, i.e. those with sizes between 2.2 and 4.0 arcsec, need to probe the outer regions, hence we constructed them up to 5 arcmin from the centre of the cluster. Once all annuli were produced, and SB was derived in each of them, we averaged all the values in regular intervals of $\log_{10}(r/\mathrm{arcsec}) = 0.1$. We performed a weighted mean to obtain our best estimate of the SB and its error. Similarly, we used as clustercentric radius the mean of all radii within each interval of the binning procedure.

The SBP derived as described above is still affected by background contamination from field stars and sky background that needs to be corrected before proceeding with the analysis. The background level needs to be determined in a region well away from the cluster, and the VST data are suitable for such requirements due to the large FOV. To this purpose, we extended the annuli construction up to 300 arcsec for every SC and adopted as local background the average flux measured between 150 and 300 arcsec. This range of values is large enough to be both statistically significant and robust against fluctuations (i.e. a rich SC located within the background estimation area would have increased the sky level if the sampling regions were smaller). Finally, the background level was subtracted from each annulus in order to get a decontaminated SBP. Fig. 2 shows an

[1] A KDE is a non-parametric technique that works by smoothing data through a kernel function in order to estimate the probability density function of a random variable. We used the version available in the SCIKIT-LEARN package (Pedregosa et al. 2011).

[2] The bandwidth of the kernel is the only parameter that must be set in a KDE.

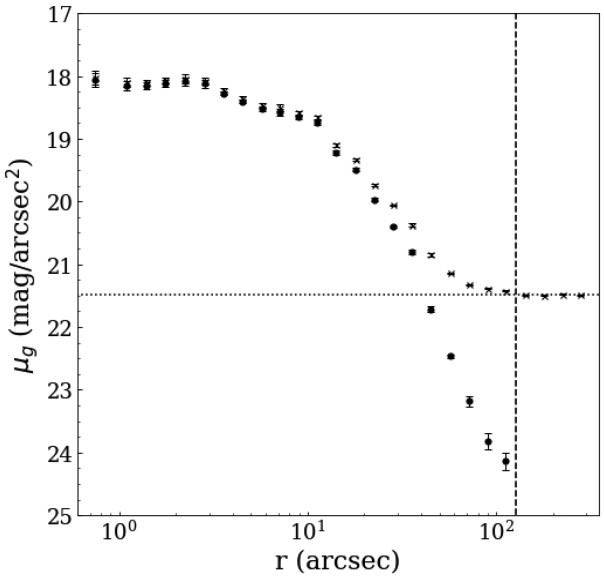

Figure 2. Example of the background subtraction procedure for NGC 419. The SBP calculated with the background contribution is displayed with crosses, while the decontaminated one is in black dots. Error bars mark the uncertainties on the SBP as defined in the text. The horizontal line represents the estimated background as described in the text. The vertical line shows the clustercentric distance where the contaminated SBP intersects the background level.

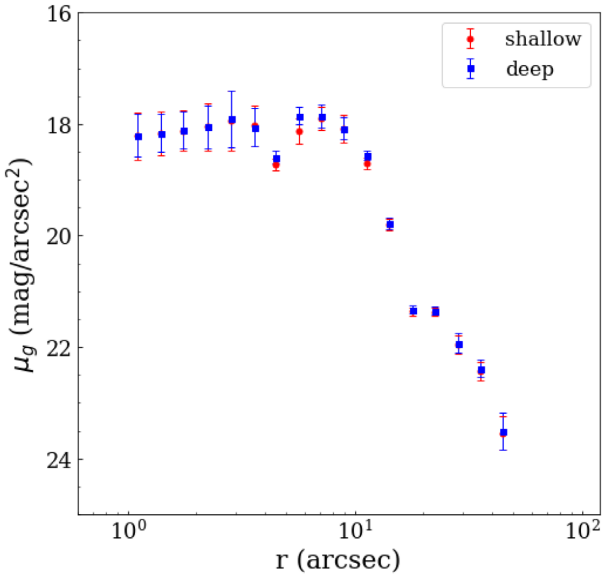

Figure 3. SBPs derived with shallow (red points) and deep (blue points) images for NGC 376.

example of the background subtraction in the case of NGC 419. In detail, the figure shows the SBPs before (crosses) and after (filled circles) the background subtraction, while the horizontal line shows the estimated background level.

Even though the procedure applied to obtain the SBP prevents saturated stars from dominating the luminosity budget (see Section 3.2), their effect must be carefully investigated. Shallow images provided us the opportunity to evaluate the impact of their presence in 11 SCs containing more than five saturated stars in the deep images, but not in the shallow ones. Fig. 3 shows the SBP derived with either shallow (red points) or deep (blue squares) images for the SC NGC 376, and, apart from some barely visible differences, the overall SBP shape is unchanged. We inspected shallow and deep images for all the 11 SCs with more than five saturated stars, not finding any remarkable difference, which led us to conclude that, with our methodology, saturated stars do not alter our SBP shapes.

4 FITTING PROCEDURE

We adopted both EFF and King profiles to fit SBPs and to derive the SC structural parameters. As the results obtained with the two different profiles are very close to each other, in the following we focus our discussion on the EFF profile in order to be consistent with previous works, since most of them adopted only the EFF profile. The interested reader can find a detailed report about the King profile in Appendix A.

4.1 EFF model

The EFF formulation is the following:

$$\mu(r) = \mu_0 + 1.25\gamma \log\left(1 + \frac{r^2}{\alpha^2}\right), \quad (1)$$

where $\mu(r)$ is the SB expressed in mag arcsec^{-2} at a given distance r from the cluster centre. μ_0, γ, and α are, respectively, the central SB, the dimensionless slope of the power law, and a parameter (expressed in arcsec) related to the core radius r_c, which is the clustercentric distance where the SB has half of its central value, through the relation

$$r_c = \alpha\sqrt{2^{2/\gamma} - 1}. \quad (2)$$

These three parameters have been derived via a non-linear least-squares method through a χ^2 minimization. As it would not be appropriate to perform the fit all along the SBP, since it extends well beyond the cluster limit, we set a limiting radius, hereafter called fitting radius (r_f), within which we executed the fit. To estimate its value we adopted the local background estimated for each cluster, and set as r_f the distance from the cluster centre where the original SBP (i.e. not subtracted) reaches it or when $\mu(r) - \Delta_\mu(r)$ is smaller than the background level in two consecutive bins. These requirements may fail when two SCs are too close in projection: the SBP increases again at the distance where the annuli begin to incorporate stars belonging to the nearby cluster. Overall, the net effect is an unrealistically large r_f, thus forcing us to set the fitting radius by hand for these SCs. The SC luminosity comes from the integration of equation (1), at the limit of r_f to infinity and yields

$$L_\infty = \frac{2\pi 10^{-0.4\mu}\alpha^2}{\gamma - 2} \quad (3)$$

provided that $\gamma > 2$, otherwise the luminosity becomes infinite.[3] To calculate the extinction-corrected total luminosity, we adopted the extinction values obtained through the procedure described in Section 5.2 when available, or the extinction maps provided by Schlegel, Finkbeiner & Davis (1998), recalibrated by Schlafly & Finkbeiner (2011), otherwise.

To convert r_c from arcsec to a real physical size expressed in parsec (pc), we need the distance modulus (DM) of the cluster. As a first approximation, we adopted the same DM for all SCs, i.e. DM = 18.98

[3]We set $\gamma = 2$ as lowest bound limit in the curve fitting to avoid negative luminosities.

mag, corresponding to the SMC centre distance, recently estimated by Graczyk et al. (2020) (see also discussion in Section 5). To be conservative, we consider an error on the DM of $\Delta DM = 0.4$ mag, corresponding to about 25 kpc at the SMC distance, in order to take into account also the depth of the SMC along the line of sight. The derived values of μ_0, α, and γ for the EFF models are listed in Table C1, while r_c and L_∞ are reported in the first column of Table 1.

We point out that for H86−6 and H86−11 we were not able to perform the fit of the *g*-band SBP because it was too noisy. For these SCs, we adopted the *i*-band SBP to derive their structural parameters.

4.2 Comparison with literature

We compared our results on the main properties of SCs with those existing in the literature for SCs in common with our sample. Since 62 SCs were analysed for the first time in this work, the comparison was carried out with the remaining ∼100. The literature studies considered here include Mackey & Gilmore (2003b), HZ06, Carvalho et al. (2008), Glatt et al. (2009), and Santos et al. (2020), who derived the main structural parameters in a homogeneous way for several SMC SCs using EFF profiles. The left-hand panel of Fig. 4 displays the comparison between our r_c obtained via the EFF profile and the literature ones, with the exception of HZ06, which will be discussed separately. To make the comparison with previous works meaningful, we homogenized the core radii, recalculating the literature values for the SMC DM we have adopted.[4] An inspection of Fig. 4 reveals that our core radii are nicely consistent within the errors with those estimated in the literature. Indeed, the average residual between our and the literature values is 0.01 ± 0.52 pc, corresponding to less than 2 per cent in terms of fractional residuals.

The right-hand panel of Fig. 4 shows the comparison between our and HZ06's core radii values. In this case, we were not able to adjust their core radii to our SMC distance, since they did not give information on their adopted distance. The figure shows that our r_c are systematically lower (-1.05 ± 3.86 pc). Although the large uncertainties prevent us from determining whether the offset is real or not, we speculate that this systematic difference might originate from the different assumption of the SMC DM by HZ06. Furthermore, their work is based on the MCPS, which is significantly shallower than the STEP survey.[5] This occurrence might be responsible for the large scatter observed between the results based on the two surveys. Indeed, also Santos et al. (2020), using data from the VISCACHA survey, found significant residuals (1.1 ± 2.7 pc, see their fig. 6), with respect to HZ06.

5 ANALYSIS OF THE CMD

In the previous section, we estimated the SC structural parameters from the study of their SBPs. In this section, we exploit the SC CMDs to extract additional fundamental physical parameters, such as the age and the mass. To this aim, the common procedure is to use the CMD to estimate the SC age from isochrone fitting and then to convert the integrated SC luminosity into total mass by adopting a mass-to-light ratio (MLR)–age–metallicity relation (e.g. Santos et al. 2020) or alternatively to use integrated colours (e.g. Roediger & Courteau 2015). However, these procedures are not usable for SCs with masses lower than ∼5000 $M_\odot$ as the stochasticity in the stellar luminosity function can produce substantial systematics in the inferred SC mass (Fouesneau & Lançon 2010; Silva-Villa & Larsen 2011; Fouesneau et al. 2014; Krumholz et al. 2015). Since our sample includes many low-mass SCs, we decided to follow a different procedure, adopting the Automated Stellar Cluster Analysis (ASTECA) open source PYTHON package (Perren, Vázquez & Piatti 2015). This tool generates synthetic SCs from a set of theoretical isochrones and performs an automatic isochrone fitting procedure. A genetic algorithm is used to find the best solution (see Perren et al. 2015, for full details). The great advantage of using ASTECA is that in practice it provides simultaneously an estimate of the age, reddening, mass, and their uncertainties by taking into account the inherently stochastic process of the isochrone fitting procedure, as a synthetic cluster is generated from a stochastically sampled initial mass function (IMF)[6] (see section 2.9.1 in Perren et al. 2015). In the following two sections, we describe the procedure employed to derive SC ages and masses.

5.1 Visual isochrone fitting

We carefully examined the CMD of each SC in our sample before running ASTECA, with the aim of performing in advance a visual isochrone fitting procedure. Such results have been used as priors for ASTECA in order to make it quicker, and to avoid that the software could catch in a local minimum, far away from the actual solution. This section describes the steps we performed to get SC ages from a visual isochrone fitting.

The CMD of a SC is contaminated by background/foreground stars belonging to the field of the host galaxy (the SMC in our case). In order to obtain reliable ages, non-cluster members should be statistically removed, especially for less populous SCs where the expected fraction of field stars are relatively high. To this aim we adopted the procedure developed by Piatti & Bica (2012), which allows us to estimate the membership probability *P* of each SC star, permitting us to carry out the isochrone comparison procedure using only stars with the highest membership probability. This method has been extensively used in literature (see e.g. Piatti et al. 2014, 2015, 2016; Ivanov et al. 2017; Gatto et al. 2020, and references therein) and proven to reduce the uncertainties in the SC parameter estimation. We made use of the PARSEC models (Bressan et al. 2012)[7] to visually identify the isochrone of a given age and metallicity[8] that best fits the distribution of SC stars with $P > 60$ per cent, in the CMD. To reduce the wide space of parameters affecting the shape of an isochrone, we fixed the DM for all SCs to DM = 18.98 mag (Graczyk et al. 2020), and we made use of an age–metallicity relation (AMR) derived for the SMC SCs (Parisi et al. 2015) to fix the metal content of the SCs, as well. Although the SMC has a considerable extension along the line of sight (see e.g. Haschke, Grebel & Duffau 2012; Subramanian & Subramaniam 2012; Jacyszyn-Dobrzeniecka et al. 2016; Ripepi et al. 2017, and references therein), we estimated the total age uncertainty of the visual fitting procedure to be $\Delta \log(t) = 0.2$ dex, which comprises both a statistical error of 0.1 dex originating from the method and a further 0.1 dex to take into account the fixed DM for the

[4] Glatt et al. (2009), Mackey & Gilmore (2003b), and Santos et al. (2020) set the SMC DM to DM = 18.88, 18.9, and 18.96 mag, respectively. Carvalho et al. (2008) did not provide information on their adopted SC distances.

[5] The MCPS has a completeness at ∼50 per cent for $V \sim 21$ (Zaritsky et al. 1997).

[6] We adopted a Kroupa (2001) IMF.

[7] http://stev.oapd.inaf.it/cgi-bin/cmd

[8] We corrected the isochrones for the adopted distance and the colour excess through the relations $g = g_{iso} + DM + R_g\, E(B-V)$ and $E(g-i) = (R_g - R_i)\, E(B-V)$ with $R_g = 3.303$ and $R_i = 1.698$ (Schlafly & Finkbeiner 2011).

Table 1. In the first column we report the SC ID as taken from Bica et al. (2020). SC properties derived through EFF models: core radius and total luminosity are in the second and third column, respectively. SC properties obtained through King's profile are listed in the fourth to the seventh column, i.e. the core radius, concentration parameter, the half-light radius, and luminosity, respectively. Then we list parameters derived through Automated Stellar Cluster Analysis (ASTECA), namely, age, reddening, metallicity, and mass. Mass-to-light ratio was derived by using the total luminosity derived from the EFF model when available, or through the King model, otherwise. Finally, in the last column, we indicate the relaxation time.

ID	EFF		King				CMD					
	r_c (pc)	$\log(L/L_\odot)$	r_c (pc)	c	r_h (pc)	$\log(L/L_\odot)$	$\log(t)$	$E(B-V)$ (mag)	Z	$\log(M/M_\odot)$	$\log(M/L)$	$\log(t_{rh})$
B10	0.2 ± 0.2	3.95 ± 0.59	0.2 ± 0.2	1.6 ± 0.8	0.7 ± 0.3	3.87 ± 0.30	$9.48^{+0.17}_{-0.39}$	0.11	0.002	$3.03^{+0.39}_{-0.58}$	− 0.92	6.86
B100	0.7 ± 0.1	4.18 ± 0.34	0.6 ± 0.1	1.0 ± 0.1	1.1 ± 0.2	4.16 ± 0.18	$8.00^{+0.15}_{-0.20}$	0.09	0.004	$3.12^{+0.23}_{-0.42}$	− 1.06	7.05
B103	0.9 ± 0.2	–	1.4 ± 0.5	0.8 ± 0.3	1.8 ± 0.5	3.87 ± 0.28	$8.24^{+0.32}_{-0.10}$	0.20	0.004	$2.95^{+0.28}_{-0.46}$	− 0.92	7.33
B105	0.8 ± 0.2	4.11 ± 0.88	0.9 ± 0.2	1.1 ± 0.2	1.6 ± 0.4	3.83 ± 0.20	$7.67^{+0.31}_{-0.23}$	0.05	0.004	$3.03^{+0.26}_{-0.44}$	− 1.08	7.26
B108	1.3 ± 0.4	–	2.0 ± 1.0	0.7 ± 0.6	2.1 ± 0.7	3.42 ± 0.34	$9.39^{+0.01}_{-0.04}$	0.06	0.002	$3.62^{+0.21}_{-0.40}$	0.20	7.79
B111	0.8 ± 0.2	–	1.2 ± 0.4	0.9 ± 0.4	1.5 ± 0.4	3.00 ± 0.25	$9.13^{+0.13}_{-0.11}$	0.12	0.002	$2.62^{+0.34}_{-0.52}$	− 0.38	7.19
B113	1.0 ± 0.3	3.52 ± 0.39	1.2 ± 0.4	0.7 ± 0.2	1.3 ± 0.3	3.47 ± 0.27	$9.04^{+0.04}_{-0.05}$	0.05	0.002	$3.29^{+0.25}_{-0.43}$	− 0.22	7.35
B115	1.0 ± 0.4	–	1.6 ± 0.8	0.8 ± 0.6	2.0 ± 0.7	4.11 ± 0.35	–	–	–	–	–	–
B117	1.0 ± 0.2	4.19 ± 0.75	1.3 ± 0.3	0.9 ± 0.2	1.8 ± 0.4	3.94 ± 0.20	$8.17^{+0.15}_{-0.24}$	0.09	0.004	$3.08^{+0.40}_{-0.59}$	− 1.11	7.37
B119	–	–	2.9 ± 2.4	0.1 ± 0.4	1.4 ± 0.4	2.95 ± 5.09	–	–	–	–	–	–
B12	–	–	2.4 ± 2.0	0.3 ± 0.6	1.7 ± 0.6	3.20 ± 0.88	$9.46^{+0.26}_{-0.09}$	0.14	0.002	$3.13^{+0.46}_{-0.64}$	− 0.07	7.49
B121	1.3 ± 0.4	4.33 ± 0.66	2.7 ± 0.8	0.3 ± 0.1	1.9 ± 0.4	4.16 ± 0.60	$7.92^{+0.18}_{-0.13}$	0.11	0.004	$2.93^{+0.28}_{-0.47}$	− 1.40	7.36
B122	2.1 ± 1.0	–	6.2 ± 4.7	0.4 ± 0.7	4.8 ± 1.7	3.83 ± 0.50	$8.21^{+0.32}_{-0.34}$	0.07	0.004	$3.30^{+0.24}_{-0.43}$	− 0.52	8.11
B124	1.2 ± 0.3	3.63 ± 0.37	2.0 ± 0.6	0.4 ± 0.2	1.6 ± 0.3	3.57 ± 0.46	$8.08^{+0.20}_{-0.35}$	0.10	0.004	$2.35^{+0.51}_{-0.70}$	− 1.29	7.06
B128	–	–	2.9 ± 1.9	0.3 ± 0.4	2.0 ± 0.6	3.52 ± 0.98	$8.02^{+0.15}_{-0.29}$	0.12	0.004	$2.71^{+0.33}_{-0.52}$	− 0.81	7.33
B137	0.8 ± 0.2	–	1.2 ± 0.3	1.0 ± 0.3	1.8 ± 0.4	3.65 ± 0.21	–	–	–	–	–	–
B165	1.1 ± 0.3	3.09 ± 0.32	1.5 ± 0.5	0.6 ± 0.2	1.5 ± 0.3	3.08 ± 0.32	–	–	–	–	–	–
B18	0.7 ± 0.2	3.29 ± 0.43	0.8 ± 0.2	0.7 ± 0.3	0.8 ± 0.2	3.20 ± 0.23	$9.72^{+0.27}_{-0.65}$	0.10	0.002	$2.93^{+0.67}_{-0.86}$	− 0.36	6.97
B21	0.8 ± 0.4	3.39 ± 2.32	2.5 ± 1.2	0.0 ± 0.2	1.1 ± 0.2	2.85 ± 6.51	$9.49^{+0.11}_{-0.49}$	0.05	0.002	$2.81^{+0.45}_{-0.63}$	− 0.57	7.05
B22	0.2 ± 0.1	–	0.3 ± 0.1	1.2 ± 0.3	0.6 ± 0.1	3.27 ± 0.21	$9.97^{+0.09}_{-0.24}$	0.12	0.002	$3.42^{+0.53}_{-0.71}$	0.16	6.95
B26	0.6 ± 0.2	2.98 ± 0.87	1.5 ± 0.5	0.2 ± 0.2	0.9 ± 0.2	2.67 ± 1.09	–	–	–	–	–	–
B34A	0.8 ± 0.3	3.55 ± 0.30	1.7 ± 0.9	0.3 ± 0.3	1.1 ± 0.3	3.55 ± 1.29	–	–	–	–	–	–
B39	1.5 ± 0.3	–	2.2 ± 0.6	0.9 ± 0.3	2.9 ± 0.6	4.09 ± 0.22	$8.67^{+0.20}_{-0.04}$	0.13	0.004	$3.39^{+0.26}_{-0.45}$	− 0.70	7.85
B52	4.1 ± 1.3	–	10.6 ± 8.1	0.3 ± 0.6	6.3 ± 2.1	4.40 ± 1.15	–	–	–	–	–	–
B65	1.3 ± 0.2	4.49 ± 0.26	1.4 ± 0.3	0.6 ± 0.1	1.5 ± 0.3	4.48 ± 0.22	–	–	–	–	–	–
B70	0.5 ± 0.1	3.74 ± 1.01	0.5 ± 0.1	1.7 ± 0.1	1.4 ± 0.2	3.45 ± 0.15	$9.64^{+0.14}_{-0.19}$	0.07	0.002	$2.97^{+0.42}_{-0.61}$	− 0.77	7.30
B71	1.8 ± 0.4	4.65 ± 0.24	2.8 ± 0.7	0.4 ± 0.1	2.2 ± 0.4	4.66 ± 0.51	$7.53^{+0.28}_{-0.18}$	0.13	0.004	$3.01^{+0.25}_{-0.44}$	− 1.63	7.45
B79	1.3 ± 0.3	4.56 ± 0.60	1.3 ± 0.4	1.1 ± 0.3	2.3 ± 0.5	4.45 ± 0.22	$7.70^{+0.32}_{-0.25}$	0.05	0.004	$2.98^{+0.25}_{-0.43}$	− 1.57	7.49
B80	0.6 ± 0.3	–	0.9 ± 0.4	1.0 ± 0.6	1.4 ± 0.5	3.52 ± 0.32	$9.08^{+0.27}_{-0.18}$	0.14	0.002	$2.84^{+0.44}_{-0.62}$	− 0.68	7.20
B9	1.0 ± 0.5	3.73 ± 1.56	2.7 ± 1.1	0.3 ± 0.2	1.8 ± 0.4	3.36 ± 0.92	–	–	–	–	–	–
B96	2.6 ± 0.5	4.24 ± 0.28	4.2 ± 1.0	0.4 ± 0.1	3.1 ± 0.6	4.21 ± 0.51	$8.27^{+0.00}_{-0.16}$	0.18	0.004	$3.26^{+0.26}_{-0.44}$	− 0.98	7.82
B97	1.4 ± 0.5	–	3.1 ± 2.1	0.3 ± 0.5	1.9 ± 0.6	3.14 ± 1.05	–	–	–	–	–	–
B99	1.4 ± 0.4	4.43 ± 0.99	1.8 ± 0.6	0.8 ± 0.3	2.3 ± 0.6	4.11 ± 0.26	$8.25^{+0.24}_{-0.32}$	0.19	0.004	$3.23^{+0.32}_{-0.51}$	− 1.20	7.62
BS 102	1.2 ± 0.4	3.73 ± 2.07	1.7 ± 0.7	0.7 ± 0.5	1.7 ± 0.4	3.17 ± 0.29	$8.37^{+0.28}_{-0.32}$	0.06	0.004	$2.56^{+0.35}_{-0.53}$	− 1.17	7.18
BS 128	–	–	1.1 ± 0.7	0.8 ± 1.3	1.0 ± 0.2	3.11 ± 0.37	$8.35^{+0.32}_{-0.36}$	0.10	0.004	$2.23^{+0.44}_{-0.62}$	− 0.89	6.73
BS 131	1.3 ± 0.3	4.04 ± 0.62	2.3 ± 1.1	0.3 ± 0.3	1.5 ± 0.3	3.83 ± 0.84	–	–	–	–	–	–
BS 138	3.5 ± 0.9	–	6.0 ± 4.8	0.4 ± 0.8	4.1 ± 1.2	3.85 ± 0.55	$9.53^{+0.03}_{-0.04}$	0.12	0.002	$3.68^{+0.22}_{-0.41}$	− 0.17	8.26
BS 2	1.1 ± 0.3	2.94 ± 0.43	1.1 ± 0.4	0.9 ± 0.4	1.6 ± 0.4	2.89 ± 0.27	–	–	–	–	–	–
BS 276	0.5 ± 0.1	4.19 ± 0.50	0.5 ± 0.1	1.2 ± 0.1	1.0 ± 0.2	4.15 ± 0.17	$8.38^{+0.24}_{-0.32}$	0.10	0.004	$3.01^{+0.28}_{-0.47}$	− 1.18	6.99
BS 76	1.7 ± 0.4	3.78 ± 0.48	1.9 ± 0.5	0.8 ± 0.3	2.4 ± 0.6	3.69 ± 0.22	$8.15^{+0.17}_{-0.27}$	0.05	0.004	$2.95^{+0.30}_{-0.49}$	− 0.83	7.53
BS 88	1.2 ± 0.4	–	2.3 ± 1.7	0.3 ± 0.6	1.3 ± 0.4	3.13 ± 0.85	$9.56^{+0.05}_{-0.16}$	0.12	0.002	$3.20^{+0.37}_{-0.55}$	0.07	7.35
H86−11	0.5 ± 0.3	–	0.9 ± 0.5	0.9 ± 0.5	1.3 ± 0.5	2.80 ± 0.37	–	–	–	–	–	–
H86−114	1.4 ± 0.3	–	2.2 ± 0.6	0.7 ± 0.3	2.5 ± 0.6	4.05 ± 0.25	$8.34^{+0.26}_{-0.37}$	0.06	0.004	$2.79^{+0.24}_{-0.42}$	− 1.26	7.50
H86−137	0.8 ± 0.2	4.28 ± 1.05	0.9 ± 0.2	1.3 ± 0.2	1.5 ± 0.3	3.87 ± 0.16	$9.14^{+0.02}_{-0.01}$	0.13	0.002	$3.52^{+0.28}_{-0.47}$	− 0.76	7.50
H86−146	0.4 ± 0.2	–	0.6 ± 0.3	1.3 ± 0.4	1.4 ± 0.4	4.11 ± 0.26	–	–	–	–	–	–
H86−150	0.9 ± 0.3	–	1.5 ± 0.6	0.8 ± 0.4	1.8 ± 0.5	3.91 ± 0.31	$7.62^{+0.16}_{-0.09}$	0.12	0.004	$2.92^{+0.26}_{-0.44}$	− 0.99	7.31
H86−159	1.6 ± 0.4	3.60 ± 0.43	2.0 ± 0.7	0.6 ± 0.3	2.0 ± 0.6	3.51 ± 0.30	–	–	–	–	–	–
H86−165	1.7 ± 0.7	–	2.5 ± 1.4	0.6 ± 0.6	2.6 ± 0.9	3.79 ± 0.39	$8.08^{+0.23}_{-0.26}$	0.10	0.004	$2.94^{+0.27}_{-0.46}$	− 0.85	7.57
H86−174	1.3 ± 0.3	4.64 ± 2.49	1.8 ± 0.6	0.7 ± 0.3	2.0 ± 0.5	3.85 ± 0.25	$8.58^{+0.13}_{-0.08}$	0.19	0.002	$2.92^{+0.32}_{-0.51}$	− 1.73	7.44
H86−175	0.9 ± 0.2	3.56 ± 0.19	1.3 ± 0.3	0.4 ± 0.1	0.9 ± 0.2	3.55 ± 0.51	–	–	–	–	–	–
H86−179	1.2 ± 0.5	3.72 ± 0.81	2.6 ± 1.9	0.2 ± 0.4	1.6 ± 0.4	3.53 ± 1.73	–	–	–	–	–	–
H86−181	0.5 ± 0.2	4.23 ± 0.81	0.6 ± 0.2	1.2 ± 0.3	1.1 ± 0.3	4.01 ± 0.22	–	–	–	–	–	–
H86−182	2.3 ± 0.6	4.44 ± 0.71	3.1 ± 1.1	0.6 ± 0.3	3.2 ± 0.7	4.22 ± 0.29	–	–	–	–	–	–
H86−186	1.1 ± 0.2	4.11 ± 0.33	1.2 ± 0.2	0.8 ± 0.1	1.5 ± 0.3	4.08 ± 0.19	$8.21^{+0.28}_{-0.18}$	0.11	0.004	$3.15^{+0.28}_{-0.46}$	− 0.96	7.30
H86−190	0.6 ± 0.2	–	1.0 ± 0.5	0.7 ± 0.5	1.1 ± 0.3	3.54 ± 0.32	$7.66^{+0.32}_{-0.29}$	0.05	0.004	$2.30^{+0.38}_{-0.56}$	− 1.24	6.75
H86−191	–	–	2.0 ± 1.5	0.3 ± 0.5	1.3 ± 0.4	3.28 ± 1.16	$8.04^{+0.24}_{-0.31}$	0.08	0.004	$2.53^{+0.24}_{-0.43}$	− 0.75	7.00
H86−193	1.8 ± 0.4	3.75 ± 0.49	2.3 ± 0.7	0.6 ± 0.3	1.9 ± 0.4	3.62 ± 0.25	$8.06^{+0.31}_{-0.34}$	0.14	0.004	$2.78^{+0.27}_{-0.45}$	− 0.98	7.31
H86−194	0.7 ± 0.4	–	2.3 ± 1.1	0.1 ± 0.2	1.1 ± 0.2	3.27 ± 2.82	$8.07^{+0.32}_{-0.27}$	0.07	0.004	$2.36^{+0.42}_{-0.60}$	− 0.92	6.85
H86−213	0.3 ± 0.1	–	0.5 ± 0.2	1.3 ± 0.3	1.0 ± 0.2	2.99 ± 0.20	$8.40^{+0.20}_{-0.28}$	0.12	0.004	$2.74^{+0.26}_{-0.45}$	− 0.25	6.92
H86−6	1.2 ± 0.3	2.57 ± 0.37	2.4 ± 0.9	0.2 ± 0.2	1.4 ± 0.3	2.48 ± 1.43	$9.44^{+0.07}_{-0.22}$	0.08	0.002	$2.86^{+0.34}_{-0.52}$	0.29	7.24
H86−60	–	–	1.5 ± 1.1	0.3 ± 0.5	0.9 ± 0.3	2.84 ± 1.24	–	–	–	–	–	–
H86−74	0.9 ± 0.2	4.77 ± 0.82	1.0 ± 0.2	1.1 ± 0.2	1.7 ± 0.3	4.51 ± 0.18	$7.92^{+0.12}_{-0.14}$	0.14	0.004	$2.66^{+0.37}_{-0.56}$	− 2.10	7.20
H86−86	0.3 ± 0.1	2.83 ± 0.62	0.4 ± 0.2	0.9 ± 0.4	0.6 ± 0.1	2.68 ± 0.26	–	–	–	–	–	–
H86−87	1.7 ± 0.6	–	4.1 ± 3.5	0.3 ± 0.6	2.5 ± 0.8	3.81 ± 1.07	$8.26^{+0.21}_{-0.30}$	0.15	0.004	$2.92^{+0.27}_{-0.46}$	− 0.89	7.54
H86−97	1.5 ± 0.4	–	2.7 ± 0.9	0.5 ± 0.2	2.2 ± 0.5	4.39 ± 0.35	$7.92^{+0.27}_{-0.00}$	0.22	0.004	$3.10^{+0.29}_{-0.47}$	− 1.29	7.52

Table 1 – *continued*

ID	EFF		King				CMD					
	r_c (pc)	$\log(L/L_\odot)$	r_c (pc)	c	r_h (pc)	$\log(L/L_\odot)$	$\log(t)$	$E(B-V)$ (mag)	Z	$\log(M/M_\odot)$	$\log(M/L)$	$\log(t_{rh})$
HW 10	3.0 ± 0.7	–	4.4 ± 1.4	0.8 ± 0.3	5.7 ± 1.4	3.92 ± 0.26	$9.59^{+0.25}_{-0.09}$	0.09	0.002	$4.29^{+0.37}_{-0.56}$	0.38	8.72
HW 11	3.6 ± 1.3	–	5.4 ± 2.5	0.9 ± 0.6	7.1 ± 2.3	4.22 ± 0.36	–	–	–	–	–	–
HW 14	7.1 ± 2.2	–	13.6 ± 10.0	0.4 ± 0.7	9.6 ± 2.7	4.27 ± 0.52	$9.50^{+0.01}_{-0.02}$	0.12	0.002	$4.23^{+0.24}_{-0.43}$	−0.04	9.03
HW 18	0.5 ± 0.1	–	0.8 ± 0.3	0.8 ± 0.3	1.0 ± 0.3	2.72 ± 0.27	–	–	–	–	–	–
HW 22	1.0 ± 0.2	3.86 ± 0.58	0.9 ± 0.2	1.3 ± 0.1	1.9 ± 0.4	3.78 ± 0.17	$9.41^{+0.03}_{-0.03}$	0.02	0.002	$3.59^{+0.26}_{-0.45}$	−0.27	7.73
HW 26	0.2 ± 0.0	4.11 ± 0.49	–	–	–	–	–	–	–	–	–	–
HW 34	–	–	1.9 ± 1.4	0.2 ± 0.5	1.0 ± 0.3	2.90 ± 2.17	$9.58^{+0.07}_{-0.09}$	0.06	0.002	$3.35^{+0.38}_{-0.56}$	0.45	7.20
HW 35	0.9 ± 0.2	3.61 ± 0.62	0.9 ± 0.2	1.1 ± 0.2	1.4 ± 0.3	3.47 ± 0.17	$8.18^{+0.31}_{-0.33}$	0.12	0.004	$2.81^{+0.29}_{-0.48}$	−0.81	7.14
HW 36	0.9 ± 0.2	3.12 ± 0.29	1.2 ± 0.5	0.5 ± 0.2	1.1 ± 0.3	3.09 ± 0.40	$9.12^{+0.19}_{-0.11}$	0.09	0.002	$2.74^{+0.48}_{-0.67}$	−0.37	7.04
HW 37	–	–	3.4 ± 2.7	0.2 ± 0.4	2.1 ± 0.6	4.15 ± 2.30	$7.60^{+0.28}_{-0.38}$	0.11	0.004	$2.30^{+0.38}_{-0.56}$	−1.84	7.21
HW 38	2.4 ± 0.7	3.64 ± 0.99	3.3 ± 1.8	0.6 ± 0.6	2.9 ± 0.9	3.38 ± 0.33	$9.59^{+0.03}_{-0.31}$	0.06	0.002	$3.72^{+0.29}_{-0.48}$	0.07	8.06
HW 40	1.6 ± 0.3	3.59 ± 0.53	1.7 ± 0.3	1.1 ± 0.1	2.9 ± 0.5	3.51 ± 0.17	$9.43^{+0.08}_{-0.04}$	0.04	0.002	$3.53^{+0.24}_{-0.43}$	−0.06	7.96
HW 41	2.8 ± 0.9	–	5.6 ± 2.3	0.8 ± 0.5	6.4 ± 1.7	3.89 ± 0.31	$9.56^{+0.06}_{-0.08}$	0.08	0.002	$3.85^{+0.24}_{-0.43}$	−0.04	8.63
HW 43	1.6 ± 0.4	–	2.6 ± 0.9	0.6 ± 0.3	2.6 ± 0.7	3.71 ± 0.29	$8.08^{+0.19}_{-0.09}$	0.06	0.004	$3.11^{+0.26}_{-0.45}$	−0.60	7.63
HW 44	1.4 ± 0.6	–	4.3 ± 3.5	0.2 ± 0.6	2.5 ± 0.8	3.57 ± 1.22	$8.63^{+0.14}_{-0.36}$	0.11	0.004	$2.71^{+0.35}_{-0.53}$	−0.87	7.51
HW 48	1.0 ± 0.2	4.06 ± 0.74	0.9 ± 0.2	1.4 ± 0.2	1.9 ± 0.4	3.90 ± 0.16	$8.11^{+0.07}_{-0.23}$	0.10	0.004	$3.01^{+0.30}_{-0.48}$	−1.05	7.40
HW 50	1.1 ± 0.7	–	3.6 ± 3.4	0.5 ± 1.0	3.0 ± 1.0	3.46 ± 0.49	$8.14^{+0.07}_{-0.26}$	0.11	0.004	$2.65^{+0.25}_{-0.44}$	−0.81	7.57
HW 52	1.9 ± 0.5	3.98 ± 0.64	4.3 ± 1.6	0.2 ± 0.2	2.6 ± 0.5	3.80 ± 1.19	$8.14^{+0.32}_{-0.22}$	0.04	0.004	$2.77^{+0.35}_{-0.54}$	−1.21	7.52
HW 53	1.3 ± 0.3	3.19 ± 0.74	2.2 ± 0.9	0.3 ± 0.3	1.3 ± 0.3	2.88 ± 0.70	$9.58^{+0.03}_{-0.19}$	0.03	0.002	$3.27^{+0.38}_{-0.57}$	0.08	7.37
HW 54	1.9 ± 0.8	–	–	–	–	–	$9.43^{+0.24}_{-0.01}$	0.11	0.002	$3.35^{+0.25}_{-0.43}$	−2.03	8.13
HW 55	2.1 ± 0.6	–	5.3 ± 2.8	0.2 ± 0.4	3.1 ± 0.8	3.50 ± 1.07	$9.19^{+0.07}_{-0.11}$	0.08	0.002	$2.86^{+0.28}_{-0.47}$	−0.64	7.75
HW 59	–	–	0.6 ± 0.2	0.2 ± 0.1	0.4 ± 0.1	2.57 ± 1.60	–	–	–	–	–	–
HW 61	1.8 ± 0.6	4.36 ± 2.27	3.7 ± 1.6	0.2 ± 0.3	2.3 ± 0.5	3.76 ± 1.10	$7.93^{+0.24}_{-0.00}$	0.11	0.004	$3.02^{+0.31}_{-0.49}$	−1.35	7.50
HW 68	0.7 ± 0.3	–	1.2 ± 0.7	0.8 ± 0.6	1.5 ± 0.5	3.06 ± 0.42	–	–	–	–	–	–
HW 74	2.3 ± 0.8	4.08 ± 1.81	3.7 ± 1.8	0.5 ± 0.4	3.3 ± 0.9	3.61 ± 0.42	$7.43^{+0.16}_{-0.32}$	0.09	0.004	$2.67^{+0.32}_{-0.51}$	−1.41	7.59
HW 78	0.8 ± 0.2	3.66 ± 0.32	0.8 ± 0.3	0.9 ± 0.2	1.2 ± 0.2	3.64 ± 0.24	$7.13^{+0.45}_{-0.11}$	0.09	0.004	$2.31^{+0.38}_{-0.57}$	−1.35	6.79
HW 8	1.0 ± 0.3	–	1.4 ± 0.4	1.4 ± 0.3	3.3 ± 0.8	4.24 ± 0.22	$7.81^{+0.18}_{-0.03}$	0.07	0.004	$3.49^{+0.24}_{-0.43}$	−0.75	7.90
HW 82	0.6 ± 0.2	–	0.8 ± 0.2	1.3 ± 0.3	1.9 ± 0.4	3.83 ± 0.20	$7.73^{+0.30}_{-0.36}$	0.07	0.004	$2.10^{+0.36}_{-0.55}$	−1.72	7.06
HW 9	1.2 ± 0.3	–	2.1 ± 0.8	0.6 ± 0.4	2.1 ± 0.6	3.18 ± 0.30	$9.52^{+0.08}_{-0.04}$	0.12	0.002	$3.48^{+0.30}_{-0.49}$	0.29	7.74
IC 1611	1.8 ± 0.4	5.28 ± 0.98	1.9 ± 0.4	1.5 ± 0.3	4.4 ± 0.9	4.97 ± 0.17	$8.21^{+0.22}_{-0.28}$	0.10	0.004	$4.07^{+0.29}_{-0.47}$	−1.21	8.34
IC 1612	3.3 ± 1.1	–	8.5 ± 6.1	0.4 ± 0.7	6.2 ± 1.9	4.65 ± 0.50	$8.08^{+0.15}_{-0.17}$	0.08	0.004	$3.25^{+0.31}_{-0.49}$	−1.39	8.25
IC1624	2.6 ± 0.5	4.86 ± 0.43	2.7 ± 0.5	0.9 ± 0.1	3.9 ± 0.7	4.81 ± 0.18	$8.31^{+0.05}_{-0.26}$	0.10	0.004	$3.80^{+0.22}_{-0.40}$	−1.06	8.17
IC 1662	2.6 ± 0.6	4.22 ± 0.46	2.7 ± 0.7	0.9 ± 0.2	4.0 ± 1.0	4.16 ± 0.23	$8.01^{+0.22}_{-0.24}$	0.10	0.004	$3.22^{+0.41}_{-0.59}$	−1.00	7.94
K1	7.8 ± 1.6	4.44 ± 0.42	9.1 ± 2.4	0.7 ± 0.3	10.2 ± 2.0	4.37 ± 0.23	$9.84^{+0.03}_{-0.20}$	0.10	0.001	$4.44^{+0.23}_{-0.42}$	−0.00	9.19
K11	3.2 ± 0.6	3.87 ± 0.31	3.5 ± 0.8	0.7 ± 0.1	4.1 ± 0.8	3.85 ± 0.23	$9.32^{+0.09}_{-0.04}$	0.16	0.002	$3.54^{+0.26}_{-0.44}$	−0.33	8.19
K13	6.0 ± 2.0	–	19.1 ± 15.5	0.2 ± 0.5	9.8 ± 3.1	4.28 ± 2.74	$9.54^{+0.05}_{-0.04}$	0.05	0.002	$4.63^{+0.24}_{-0.43}$	0.35	9.21
K15	1.8 ± 0.3	4.76 ± 0.98	1.8 ± 0.3	1.6 ± 0.2	4.0 ± 0.7	4.46 ± 0.16	$8.84^{+0.15}_{-0.39}$	0.14	0.002	$3.43^{+0.31}_{-0.49}$	−1.33	8.08
K16	2.1 ± 0.4	3.46 ± 0.31	2.9 ± 0.8	0.5 ± 0.2	2.3 ± 0.5	3.40 ± 0.35	$9.46^{+0.08}_{-0.02}$	0.05	0.002	$3.55^{+0.28}_{-0.47}$	0.08	7.83
K17	2.0 ± 0.4	4.78 ± 0.69	1.9 ± 0.3	1.4 ± 0.1	4.6 ± 0.8	4.66 ± 0.16	$8.82^{+0.08}_{-0.13}$	0.11	0.002	$3.64^{+0.27}_{-0.46}$	−1.15	8.26
K21	8.3 ± 1.7	–	10.7 ± 2.7	0.9 ± 0.3	14.8 ± 3.1	4.91 ± 0.22	$9.48^{+0.02}_{-0.31}$	0.05	0.002	$4.96^{+0.20}_{-0.39}$	0.05	9.61
K25	1.8 ± 0.6	–	2.8 ± 1.2	0.8 ± 0.5	3.5 ± 1.2	4.38 ± 0.33	$8.25^{+0.22}_{-0.32}$	0.15	0.004	$3.40^{+0.25}_{-0.43}$	−0.97	7.96
K27	3.6 ± 0.7	–	5.2 ± 1.4	0.9 ± 0.3	7.1 ± 1.6	4.56 ± 0.23	$9.13^{+0.06}_{-0.07}$	0.11	0.002	$4.03^{+0.27}_{-0.45}$	−0.53	8.72
K28	5.1 ± 0.9	4.99 ± 0.68	5.2 ± 1.0	1.2 ± 0.2	8.9 ± 1.6	4.83 ± 0.17	$9.57^{+0.03}_{-0.04}$	0.08	0.002	$4.70^{+0.23}_{-0.41}$	−0.28	9.18
K30	6.6 ± 1.8	–	10.0 ± 3.6	0.7 ± 0.4	11.7 ± 3.2	4.89 ± 0.30	$8.30^{+0.09}_{-0.30}$	0.09	0.004	$3.87^{+0.27}_{-0.45}$	−1.02	8.91
K31	13.2 ± 3.2	–	20.8 ± 8.8	0.5 ± 0.4	18.1 ± 5.7	5.28 ± 0.32	$8.63^{+0.17}_{-0.29}$	0.06	0.004	$4.24^{+0.26}_{-0.44}$	−1.05	9.37
K34	2.9 ± 0.5	4.80 ± 0.31	3.4 ± 0.6	0.6 ± 0.1	3.6 ± 0.6	4.77 ± 0.22	$8.74^{+0.06}_{-0.10}$	0.11	0.002	$3.69^{+0.24}_{-0.42}$	−1.12	8.11
K38	12.6 ± 3.2	–	19.7 ± 8.1	0.5 ± 0.4	17.7 ± 4.8	4.92 ± 0.32	$9.48^{+0.03}_{-0.05}$	0.05	0.002	$4.69^{+0.24}_{-0.43}$	−0.23	9.61
K4	4.3 ± 0.9	–	5.3 ± 1.2	1.0 ± 0.3	7.7 ± 1.5	4.17 ± 0.19	$9.70^{+0.01}_{-0.01}$	0.14	0.002	$4.11^{+0.26}_{-0.45}$	−0.06	8.86
K42	0.7 ± 0.1	4.85 ± 0.91	0.7 ± 0.1	1.5 ± 0.2	1.7 ± 0.3	4.61 ± 0.16	$7.85^{+0.14}_{-0.12}$	0.13	0.002	$2.83^{+0.30}_{-0.48}$	−2.02	7.25
K43	2.3 ± 0.5	–	3.5 ± 1.1	0.8 ± 0.3	4.5 ± 1.1	4.40 ± 0.26	$8.21^{+0.18}_{-0.02}$	0.16	0.004	$3.61^{+0.25}_{-0.43}$	−0.79	8.19
K44	11.4 ± 2.5	4.77 ± 0.48	13.3 ± 3.9	0.8 ± 0.3	15.7 ± 3.7	4.68 ± 0.24	$9.57^{+0.08}_{-0.06}$	0.09	0.002	$5.09^{+0.29}_{-0.47}$	0.32	9.71
K45w	1.6 ± 0.4	3.82 ± 0.37	2.2 ± 0.6	0.6 ± 0.2	2.2 ± 0.5	3.78 ± 0.31	$8.20^{+0.17}_{-0.41}$	0.08	0.004	$2.72^{+0.29}_{-0.47}$	−1.10	7.39
K47	1.7 ± 0.4	4.47 ± 0.33	1.8 ± 0.5	0.8 ± 0.2	2.4 ± 0.5	4.44 ± 0.23	$7.42^{+0.09}_{-0.03}$	0.03	0.004	$3.17^{+0.29}_{-0.48}$	−1.29	7.55
K5	3.6 ± 0.7	4.83 ± 0.69	3.7 ± 0.7	1.2 ± 0.2	6.6 ± 1.2	4.67 ± 0.17	$9.14^{+0.03}_{-0.01}$	0.15	0.002	$4.18^{+0.23}_{-0.42}$	−0.65	8.73
K50	2.6 ± 0.5	4.74 ± 0.60	3.4 ± 1.1	0.6 ± 0.3	3.0 ± 0.7	4.54 ± 0.27	$7.38^{+0.09}_{-0.26}$	0.09	0.004	$3.36^{+0.23}_{-0.41}$	−1.38	7.77
K53	2.3 ± 0.8	–	8.3 ± 2.5	0.1 ± 0.1	4.0 ± 0.7	4.28 ± 2.83	$8.07^{+0.09}_{-0.09}$	0.07	0.004	$2.93^{+0.25}_{-0.43}$	−1.35	7.85
K54	2.9 ± 0.7	4.58 ± 0.31	3.1 ± 0.9	0.7 ± 0.2	3.8 ± 1.0	4.56 ± 0.26	–	–	–	–	–	–
K55	2.4 ± 0.6	4.67 ± 1.03	2.9 ± 0.8	1.1 ± 0.3	4.9 ± 1.1	4.32 ± 0.22	$8.48^{+0.11}_{-0.23}$	0.13	0.004	$3.35^{+0.26}_{-0.45}$	−1.32	8.16
K56	2.2 ± 0.5	–	3.1 ± 0.9	0.8 ± 0.3	3.8 ± 0.8	4.26 ± 0.24	$7.90^{+0.23}_{-0.21}$	0.11	0.004	$3.33^{+0.24}_{-0.43}$	−0.93	7.95
K57	2.4 ± 0.6	–	4.2 ± 2.2	0.5 ± 0.5	3.1 ± 0.8	3.89 ± 0.38	$8.53^{+0.02}_{-0.05}$	0.09	0.004	$3.24^{+0.26}_{-0.45}$	−0.65	7.84
K61	2.0 ± 0.6	–	5.0 ± 2.3	0.3 ± 0.3	3.4 ± 0.8	4.10 ± 0.81	$7.96^{+0.49}_{-0.33}$	0.13	0.004	$2.67^{+0.33}_{-0.52}$	−1.43	7.64
K63	1.5 ± 0.5	–	2.4 ± 0.9	0.8 ± 0.3	2.9 ± 0.8	4.06 ± 0.29	$8.07^{+0.29}_{-0.26}$	0.08	0.004	$3.16^{+0.29}_{-0.47}$	−0.90	7.72
K8	2.4 ± 0.5	–	3.4 ± 1.0	0.9 ± 0.3	4.6 ± 1.1	3.89 ± 0.24	$9.45^{+0.02}_{-0.00}$	0.12	0.002	$3.65^{+0.25}_{-0.43}$	−0.24	8.32
K9	2.9 ± 0.9	–	6.3 ± 2.3	0.6 ± 0.4	6.5 ± 1.7	3.91 ± 0.29	$8.85^{+0.09}_{-0.06}$	0.09	0.002	$3.52^{+0.26}_{-0.45}$	−0.39	8.44
L14	2.8 ± 0.7	4.20 ± 1.18	3.7 ± 1.1	0.8 ± 0.3	4.7 ± 1.1	3.76 ± 0.25	$9.38^{+0.11}_{-0.03}$	0.13	0.002	$3.65^{+0.24}_{-0.42}$	−0.55	8.32
L19	4.5 ± 1.7	–	–	–	–	–	$9.55^{+0.03}_{-0.05}$	0.19	0.002	$3.85^{+0.32}_{-0.50}$	−2.08	8.67
L28	1.3 ± 0.3	4.38 ± 0.62	1.3 ± 0.3	1.2 ± 0.1	2.8 ± 0.5	4.28 ± 0.17	–	–	–	–	–	–
L31	1.6 ± 0.3	4.49 ± 1.03	1.7 ± 0.3	1.3 ± 0.2	3.3 ± 0.6	4.12 ± 0.17	–	–	–	–	–	–
L33	1.7 ± 0.4	4.28 ± 0.71	1.9 ± 0.5	1.0 ± 0.3	3.1 ± 0.7	4.10 ± 0.23	–	–	–	–	–	–
L48	1.6 ± 0.3	4.48 ± 0.31	1.6 ± 0.4	0.9 ± 0.1	2.3 ± 0.4	4.46 ± 0.20	$7.63^{+0.20}_{-0.05}$	0.09	0.004	$3.40^{+0.21}_{-0.40}$	−1.08	7.63

Table 1 – *continued*

ID	EFF		King				CMD					
	r_c (pc)	$\log(L/L_\odot)$	r_c (pc)	c	r_h (pc)	$\log(L/L_\odot)$	$\log(t)$	$E(B-V)$ (mag)	Z	$\log(M/M_\odot)$	$\log(M/L)$	$\log(t_{rh})$
L51	1.3 ± 0.3	4.93 ± 1.29	1.7 ± 0.5	1.0 ± 0.3	2.6 ± 0.7	4.45 ± 0.23	$7.48^{+0.23}_{-0.24}$	0.02	0.004	$3.21^{+0.25}_{-0.44}$	− 1.72	7.64
L52	1.1 ± 0.2	4.15 ± 0.61	1.1 ± 0.2	1.2 ± 0.2	2.0 ± 0.4	4.04 ± 0.17	$8.31^{+0.08}_{-0.10}$	0.02	0.004	$3.23^{+0.30}_{-0.48}$	− 0.92	7.52
L56	1.1 ± 0.2	5.10 ± 0.38	1.0 ± 0.2	1.1 ± 0.1	1.9 ± 0.4	5.07 ± 0.18	$7.65^{+0.15}_{-0.25}$	0.05	0.004	$3.41^{+0.22}_{-0.41}$	− 1.69	7.50
L65	2.0 ± 0.8	–	4.6 ± 2.9	0.7 ± 0.7	5.0 ± 2.2	4.37 ± 0.44	$7.84^{+0.18}_{-0.24}$	0.11	0.004	$3.24^{+0.23}_{-0.42}$	− 1.13	8.09
L66	1.3 ± 0.2	4.85 ± 0.33	1.3 ± 0.3	0.8 ± 0.1	1.7 ± 0.3	4.82 ± 0.19	$7.44^{+0.25}_{-0.23}$	0.05	0.004	$3.21^{+0.27}_{-0.45}$	− 1.64	7.36
L80	3.2 ± 0.7	–	4.7 ± 1.4	0.8 ± 0.3	5.8 ± 1.3	4.45 ± 0.24	$8.34^{+0.04}_{-0.01}$	0.05	0.004	$3.57^{+0.23}_{-0.41}$	− 0.88	8.34
L91	3.6 ± 0.8	4.37 ± 0.69	5.2 ± 1.8	0.5 ± 0.3	4.5 ± 1.0	4.12 ± 0.30	$9.15^{+0.10}_{-0.02}$	0.19	0.002	$3.60^{+0.26}_{-0.44}$	− 0.77	8.26
L93	3.4 ± 0.6	3.93 ± 0.47	3.8 ± 0.9	0.8 ± 0.2	4.3 ± 0.8	3.83 ± 0.20	$9.43^{+0.22}_{-0.21}$	0.06	0.002	$3.32^{+0.26}_{-0.45}$	− 0.60	8.16
NGC 152	6.4 ± 1.2	5.20 ± 0.74	6.7 ± 1.4	1.2 ± 0.3	11.2 ± 2.1	4.99 ± 0.18	$9.15^{+0.03}_{-0.02}$	0.13	0.002	$4.80^{+0.23}_{-0.41}$	− 0.40	9.32
NGC 176	3.1 ± 0.7	4.56 ± 0.37	3.5 ± 0.9	0.8 ± 0.2	4.3 ± 0.9	4.52 ± 0.23	$8.11^{+0.01}_{-0.04}$	0.07	0.004	$3.54^{+0.22}_{-0.41}$	− 1.02	8.12
NGC 220	2.9 ± 0.6	5.11 ± 0.72	2.9 ± 0.6	1.3 ± 0.3	6.2 ± 1.3	4.95 ± 0.18	$8.08^{+0.13}_{-0.26}$	0.08	0.004	$3.90^{+0.24}_{-0.43}$	− 1.21	8.49
NGC 222	2.4 ± 0.6	–	3.2 ± 0.9	1.1 ± 0.3	5.8 ± 1.5	4.90 ± 0.22	$7.92^{+0.20}_{-0.24}$	0.09	0.004	$3.79^{+0.24}_{-0.42}$	− 1.12	8.40
NGC 231	2.9 ± 0.7	–	4.3 ± 1.3	1.0 ± 0.3	7.2 ± 2.2	4.82 ± 0.25	$7.94^{+0.27}_{-0.15}$	0.06	0.004	$3.84^{+0.23}_{-0.41}$	− 0.99	8.55
NGC 241	1.8 ± 0.4	4.71 ± 0.62	1.8 ± 0.4	1.2 ± 0.3	3.5 ± 0.8	4.60 ± 0.20	$7.84^{+0.09}_{-0.21}$	0.07	0.004	$3.57^{+0.25}_{-0.43}$	− 1.14	7.98
NGC 242	1.4 ± 0.4	–	1.9 ± 0.5	1.1 ± 0.3	3.5 ± 0.9	4.59 ± 0.22	$7.78^{+0.10}_{-0.24}$	0.07	0.004	$3.27^{+0.28}_{-0.46}$	− 1.31	7.87
NGC 256	1.8 ± 0.4	4.72 ± 0.23	3.0 ± 0.7	0.3 ± 0.1	2.2 ± 0.4	4.74 ± 0.56	$7.92^{+0.00}_{-0.01}$	0.13	0.004	$3.13^{+0.29}_{-0.47}$	− 1.59	7.52
NGC 265	2.9 ± 0.5	5.11 ± 0.49	3.0 ± 0.6	1.0 ± 0.1	4.7 ± 0.9	5.04 ± 0.18	$8.40^{+0.05}_{-0.13}$	0.16	0.004	$3.85^{+0.25}_{-0.43}$	− 1.26	8.32
NGC 269	1.8 ± 0.3	4.80 ± 0.70	1.8 ± 0.3	1.3 ± 0.1	3.7 ± 0.6	4.66 ± 0.16	–	–	–	–	–	–
NGC 290	0.7 ± 0.2	–	0.9 ± 0.3	1.4 ± 0.3	2.3 ± 0.5	4.96 ± 0.20	$7.93^{+0.56}_{-0.00}$	0.19	0.004	$3.76^{+0.32}_{-0.50}$	− 1.20	7.78
NGC 294	2.3 ± 0.4	4.92 ± 0.40	2.4 ± 0.4	0.9 ± 0.1	3.5 ± 0.6	4.88 ± 0.17	$8.70^{+0.03}_{-0.01}$	0.08	0.004	$3.81^{+0.25}_{-0.44}$	− 1.10	8.14
NGC 299	1.3 ± 0.3	4.98 ± 0.38	1.3 ± 0.3	0.8 ± 0.1	1.8 ± 0.4	4.94 ± 0.19	$7.65^{+0.15}_{-0.12}$	0.04	0.004	$3.05^{+0.24}_{-0.43}$	− 1.93	7.36
NGC 306	1.7 ± 0.4	4.71 ± 0.41	2.9 ± 0.9	0.4 ± 0.2	2.3 ± 0.5	4.66 ± 0.46	$7.77^{+0.13}_{-0.17}$	0.10	0.004	$3.27^{+0.24}_{-0.43}$	− 1.44	7.60
NGC 330	3.1 ± 0.6	6.08 ± 0.55	3.0 ± 0.6	1.3 ± 0.1	6.6 ± 1.2	6.01 ± 0.17	$7.29^{+0.22}_{-0.23}$	0.14	0.004	$4.61^{+0.23}_{-0.41}$	− 1.46	8.77
NGC 361	4.8 ± 0.9	5.09 ± 0.62	5.0 ± 0.9	1.1 ± 0.1	8.3 ± 1.5	4.95 ± 0.17	$9.49^{+0.02}_{-0.01}$	0.07	0.002	$4.49^{+0.25}_{-0.44}$	− 0.60	9.03
NGC 376	2.4 ± 0.6	5.32 ± 0.37	2.4 ± 0.7	0.9 ± 0.2	3.8 ± 0.8	5.29 ± 0.22	$7.42^{+0.05}_{-0.13}$	0.11	0.004	$4.10^{+0.21}_{-0.40}$	− 1.22	8.21
NGC 416	2.4 ± 0.5	5.45 ± 0.78	2.3 ± 0.5	1.6 ± 0.3	6.1 ± 1.2	5.30 ± 0.17	$9.79^{+0.03}_{-0.04}$	0.12	0.002	$4.81^{+0.26}_{-0.44}$	− 0.64	9.00
NGC 419	3.6 ± 0.6	5.72 ± 0.57	3.3 ± 0.6	1.3 ± 0.1	7.9 ± 1.4	5.65 ± 0.16	$9.13^{+0.00}_{-0.04}$	0.09	0.002	$5.16^{+0.22}_{-0.40}$	− 0.56	9.25
OGLE 132	–	–	2.5 ± 1.9	0.4 ± 0.6	1.8 ± 0.6	3.55 ± 0.59	$9.09^{+0.21}_{-0.09}$	0.14	0.002	$2.95^{+0.40}_{-0.58}$	− 0.60	7.42
OGLE 172	0.5 ± 0.2	2.66 ± 0.31	1.7 ± 0.5	0.0 ± 0.1	0.7 ± 0.1	2.60 ± 5.67	–	–	–	–	–	–
OGLE 28	0.6 ± 0.2	–	1.1 ± 0.6	0.6 ± 0.5	1.1 ± 0.3	2.94 ± 0.39	–	–	–	–	–	–
OGLE 5	0.6 ± 0.2	2.31 ± 0.39	1.7 ± 0.7	0.0 ± 0.2	0.7 ± 0.1	2.20 ± 4.91	–	–	–	–	–	–
OGLE 53	0.9 ± 0.3	–	2.4 ± 1.9	0.1 ± 0.5	1.0 ± 0.3	3.39 ± 3.54	–	–	–	–	–	–
OGLE 6	0.2 ± 0.1	–	0.3 ± 0.1	1.1 ± 0.3	0.6 ± 0.2	2.67 ± 0.22	$9.59^{+0.14}_{-0.40}$	0.08	0.002	$2.86^{+0.57}_{-0.75}$	0.19	6.71
RZ 140	1.3 ± 0.4	–	2.0 ± 0.8	0.7 ± 0.4	2.3 ± 0.7	3.21 ± 0.32	$9.13^{+0.05}_{-0.04}$	0.09	0.002	$3.15^{+0.25}_{-0.44}$	− 0.06	7.66
RZ 82	1.1 ± 0.2	3.24 ± 0.69	1.3 ± 0.4	0.8 ± 0.3	1.6 ± 0.3	3.02 ± 0.22	–	–	–	–	–	–

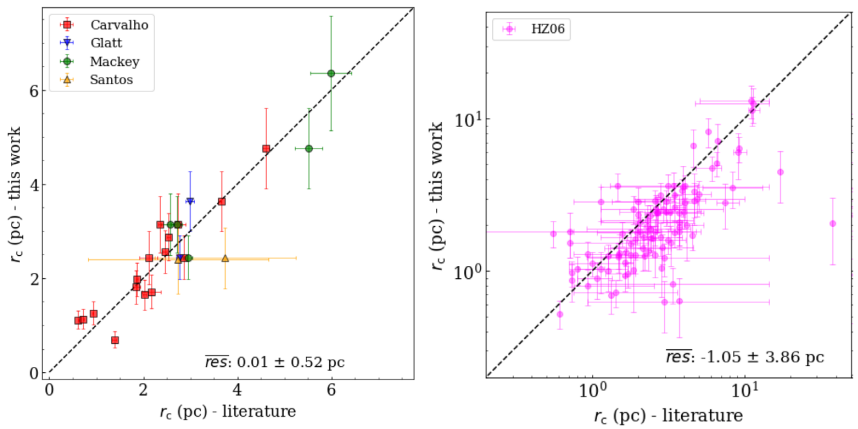

Figure 4. Left: comparison of our core radii (y-axis) with values in the literature (x-axis). Different works are marked with different colours. Right: comparison of our core radii with those taken from HZ06. Note that this panel is in logarithmic scale.

galaxy.[9] We varied the age and reddening of the isochrones looking for the one best matching the following key evolutionary sequences: main sequence (MS), turn-off (TO) point, subgiant branch, blue loop (BL), and red clump (RC). These sequences have been used to aid the visual fitting procedure, which was performed by the authors independently, in order to check the resulting reliability/uncertainty. For 36 SCs we were not able to derive even a rough estimate of the age, as their CMDs present none or too few stars on the above quoted key evolutionary stellar phases. Therefore, we conservatively decided to exclude them from the analysis with ASteCA. For these 36 clusters we only provide the structural parameters derived through the study of their SBPs.

[9]An error of 0.1 dex in the age estimate is the result of a ΔDM $\sim$ 0.4 mag at the SMC distance.

5.2 Analysis of the CMD with ASteCA

The 134 SCs with an age estimate from visual isochrone fitting of their CMD have been further analysed with ASteCA with the main scope of deriving their ages and masses and the proper uncertainties by means of an objective methodology.[10] To use the ASteCA package we have first to define a list of priors for the relevant SC quantities to be estimated. In more detail, we fixed the metallicity as already done in Section 5.1 but we let the DM vary in the $18.6 \leq \mathrm{DM} \leq 19.2$ mag interval,[11] in order to correct any bias we introduced in the visual fitting procedure by fixing it. The reddening values were allowed to vary in the range $0 \leq E(B-V) \leq 0.3$ mag. Priors on the SC ages were of $\log(t) \pm 0.6$ dex, (i.e. 3σ), around the age estimated in the previous section through the visual fitting procedure. Finally, we allowed the SC total mass to vary over a large interval, i.e. $10 \leq (M/\mathrm{M}_{\odot}) \leq 10^6$.[12] Results from the CMD fitting by means of the ASteCA package are listed in Table 1.

5.3 Comparison with previous studies

We compared the ages derived from our CMDs with those present in the literature. To this aim we selected the works by Chiosi et al. (2006), Glatt, Grebel & Koch (2010), Perren, Piatti & Vázquez (2017), and Nayak et al. (2018) who presented ages for a significant number of SCs using the isochrone fitting procedure (visual or automatic). We note that Nayak et al.'s (2018) errors are between 0.24 and 0.26 dex in $\log(t)$, hence we adopted a mean of 0.25 dex for all their SCs, while for Glatt et al.'s (2010) SCs we adopted a mean error of 0.3 dex, i.e. their lowest error. The left-hand panel of Fig. 5 shows the comparison between our results and those by Chiosi et al. (2006), Glatt et al. (2010), and Nayak et al. (2018). It can be clearly seen that, except for a few cases, our age estimates are in very good agreement with those from the literature up to 1 Gyr, whereas for older ages, the difference becomes noticeable. This discrepancy is likely due to the too shallow photometry analysed in the quoted works, which makes it unfeasible to correctly detect the MS TO for clusters older than 1 Gyr. Indeed, Glatt et al. (2010) pointed out the difficulty to derive ages of intermediate-age clusters with their MCPS data (see their section 2). In contrast, the comparison with Perren et al. (2017),[13] displayed in the right-hand panel of Fig. 5, shows very good agreement for the whole range of ages derived in this work. Concerning the estimated total masses, Fig. 6 (left-hand panel) shows the comparison between our results and those by Maia, Piatti & Santos (2014) and Song et al. (2021) for the samples of SCs in common. Maia et al. (2014) provided SC masses derived through star counts integrated down to 0.1 $\mathrm{M}_{\odot}$, while Song et al. (2021) obtained dynamical masses through spectroscopic measurements of radial velocities of the individual member stars. The figure shows a very good agreement between this work and the two quoted investigations, with an average of the residuals (our work minus literature) equal to -0.06 ± 0.34 dex, i.e. without any systematic difference over a very broad range of masses, down to few hundreds of solar masses. In addition, we also considered the works by Mackey & Gilmore (2003b), Carvalho et al. (2008), and Santos et al. (2020), which provided mass estimates trough a MLR by using the total cluster luminosity estimated from the EFF model fitting. The result of this comparison is presented in the right-hand panel of Fig. 6, which shows an overall overestimate of the masses in the aforementioned investigations with respect to this work, even if a relatively high scatter. The comparison of the masses with four SCs in common between Song et al. (2021), Mackey & Gilmore (2003b), and Carvalho et al. (2008) revealed that the latter two works derived larger masses also with respect to the dynamical estimates, i.e. $\Delta\log M = 0.37$ dex for Mackey & Gilmore (2003b) and $\Delta\log M = 0.27$ dex for Carvalho et al. (2008). As dynamical masses are more reliable than those derived through integrated properties, the good agreement displayed in the left-hand panel of the figure makes us confident about our mass assessment.

[10] We adopted the same set of PARSEC isochrones utilized in Section 5.1.
[11] All priors indicated in the text are flat.
[12] We checked that estimated masses did not change within uncertainties with a different prior selection.
[13] Their data set consists of CT1 Washington photometry, compiled on the basis of 19 previous works.

6 RESULTS

The SC parameters derived from the SBP fitting are shown in Table C1, along with the radius fitting, the coordinates, and the tile hosting the SC. The physical SC parameters, like their sizes, luminosities, and masses, are, instead, listed in Table 1. The best-fitting profiles for all SCs are depicted in Fig. D1 for both EFF and King models. Again, throughout this section, we provide results obtained with the EFF profiles. For completeness, a discussion about quantities obtained with the King profile is presented in Appendix A.

6.1 Core radius evolution with age: is it mass dependent?

An expansion of the core radius is expected to take place after a few hundreds of Myr. Besides the MCs, Ryon et al. (2015) analysed a large sample of young ($\log(t) \leq 8.5$) and massive ($\log(M/\mathrm{M}_{\odot}) \geq 10^4$) SCs in M83, and found evidence of an increasing trend between core radius and age. Ryon et al. (2017) noticed a similar trend in NGC 628 and NGC 1313 again with a sample of young massive SCs (i.e. $\log(M/\mathrm{M}_{\odot}) \geq 5 \times 10^3$ and $t \leq 200$ Myr). Both works indicated the mass loss by stellar evolution as the candidate physical mechanism responsible for the presence of such core radius–age relationship. Chandar et al. (2016) studied 3816 SCs in M51, finding again an expansion during their early life. San Roman et al. (2012), on the basis of the study of 161 SCs in M33, depicted a trend quite similar to the one observed in the LMC by Elson et al. (1989), Elson (1991, 1992), Mackey & Gilmore (2003a), namely an increasing core radius spread with age (see e.g. fig. 14 in Mackey & Gilmore 2003a). A hint for a similar behaviour was found for the first time in the SMC by Mackey & Gilmore (2003b) based on a sample of 10 SCs. More recently, Carvalho et al. (2008) and Santos et al. (2020), investigated a larger but still rather small sample of 23 and 25 SMC SCs, respectively, observing a larger spread of the core radius for SCs older than $\log(t) \sim 8.5$ dex with respect to young SCs (e.g. fig. 14 in Santos et al. 2020). The current scenario assumes that, besides an expansion in the early SC life likely due to mass loss from stellar evolution, another inner physical process triggers some SCs to increase their core radius as they get older than $\log(t) = 8.0$–8.5 dex, but what the actual mechanism is and why it affects only a fraction of the SCs is still an open question. In Fig. 7, we show the r_c as a function of the SC ages, colour coded according to their estimated mass for the sample of 134 SCs investigated in this work. To widen the sample and to augment the probed age interval, we also plotted in the same figure LMC and SMC SCs analysed by Mackey & Gilmore (2003a,b), so that the total sample of SCs displayed in the figure is 185 objects. An inspection of Fig. 7 confirms that SCs younger than ∼200–300 Myr ($\log(t) \sim 8.3$–8.5 dex) are all compact with

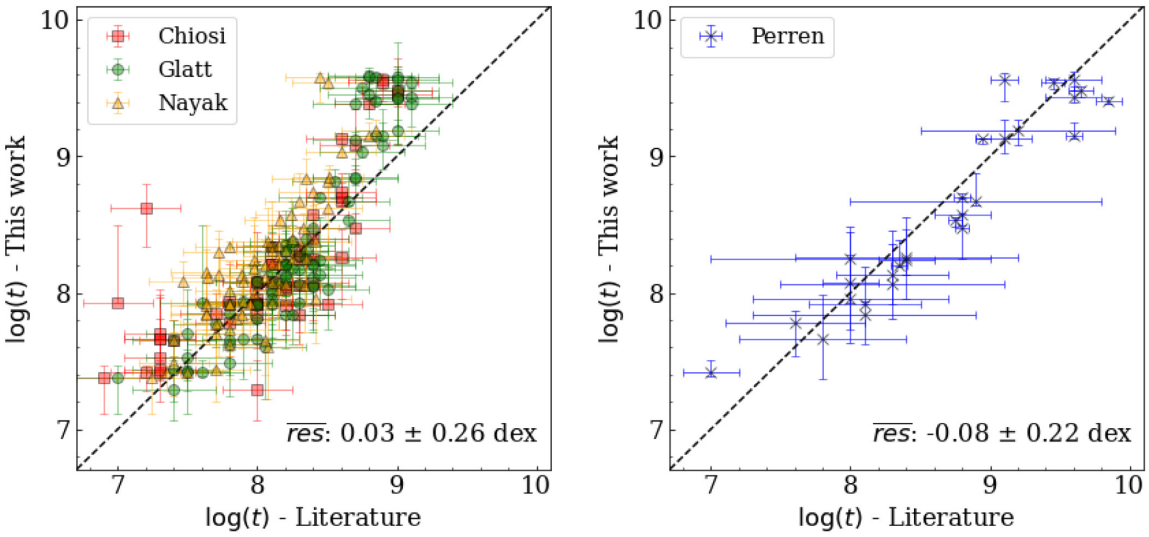

Figure 5. Comparison between our age estimates (*y*-axis) with those taken from the literature (*x*-axis). Different works are marked with different colours. The black dashed line indicates the one-to-one relationship. Residuals are to be read as our work minus literature. Note that residuals in the left-hand panel have been calculated using only SCs younger than 1 Gyr.

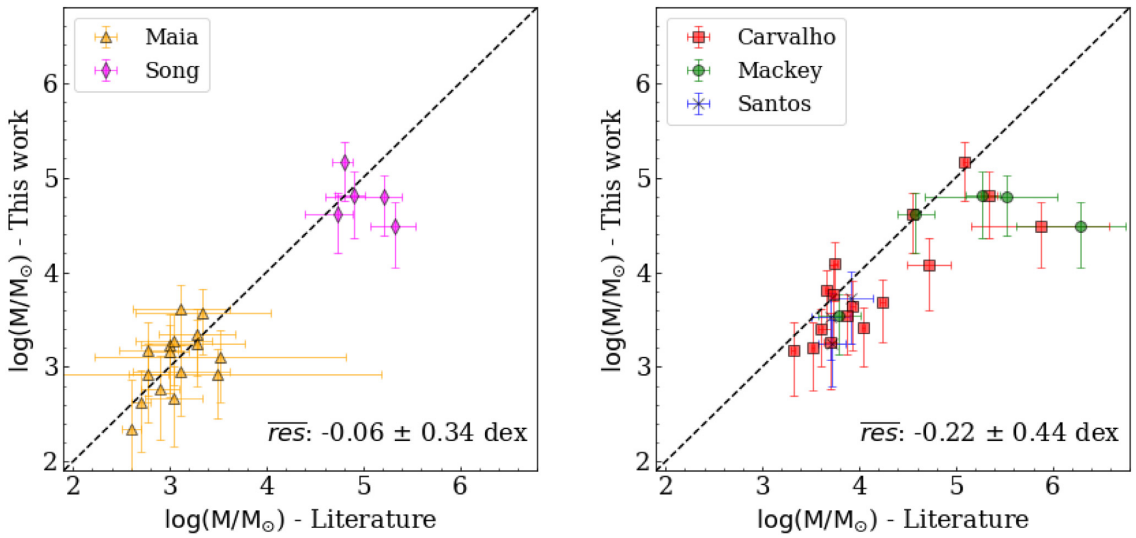

Figure 6. Comparison between our mass estimates (*y*-axis) with those taken from the literature (*x*-axis). Different works are marked with different colours. The black dashed line indicates the one-to-one relationship. Residuals are to be read as our work minus literature.

no exception.[14] More precisely, an early expansion in the first 10–20 Myr seems to be present. This early expansion has been detected also in stellar systems beyond the MCs (e.g. Ryon et al. 2015, 2017; Chandar et al. 2016), and is thought to be caused by mass loss from stellar evolution.

After this rapid phase of expansion, for the next 200–300 Myr the core radius does not seem to experience any further alteration. Beyond $t \sim$200 Myr a few SCs with $r_c > 3.5$ pc appear, while at $t \geq 1$ Gyr the fraction of SCs with $r_c > 3.5$ pc become significant. Hence, a different process with respect to that responsible for the early expansion must be invoked to explain the core radius expansion at ages later than $t \sim 200$ Myr. In the following we refer to this feature as core radius–age relationship, as done in previous works. This behaviour has been explained by Elson et al. (1987) and Mackey & Gilmore (2003a) as a real evolution during the SCs lifetime. Taking advantage of the larger number and wider range in mass of our SC sample we may put constraints on the physics behind the core radius expansion.

First of all, the fraction of SCs having $\log(t) \geq 8.25$ and $r_c \geq 3.5$ pc are ∼0.28. If this fraction were constant all along the SC lifetime, we would expect about 22 young SCs with a large core radius, hence the complete lack of them is significant at more than the 4σ level.

A closer inspection of Fig. 7 also suggests that the majority of the SCs with large core radii are also very massive. We wonder whether the mass could be, in first approximation, the physical parameter that drives intermediate-age SCs to expand their inner regions. To better investigate this hypothesis, in Fig. 8, we split up the r_c–age plot into two different mass intervals. The difference between the two panels is remarkable: in the high mass range (i.e. $M \geq 10^{3.5}$ M$_\odot$,

[14] Actually, three SCs reach 3.5 pc at 1σ.

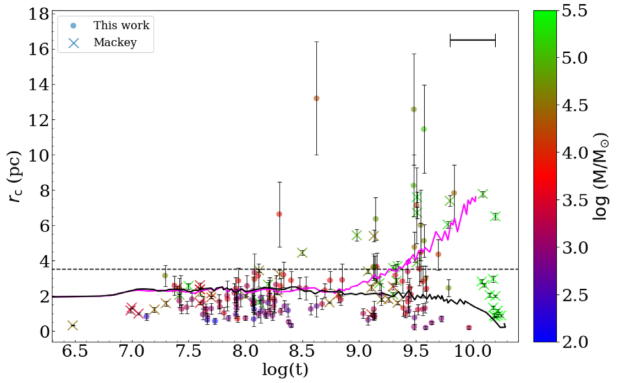

Figure 7. Core radius, estimated via an EFF profile, versus the SC age. Filled circles indicate SCs analysed in this work, while crosses represent SCs studied by Mackey & Gilmore (2003a,b). All SCs are colour coded according to their mass. In order to keep the figure readable, we do not draw the errors on the x-axis. A typical age error bar of $\Delta\log(t) = 0.2$ dex is shown in the upper right-hand corner. The horizontal dashed line is at 3.5 pc. The two solid lines represent the results of N-body simulations extrapolated from Mackey et al. (2008), for a case with no primordial mass segregation and a fraction of retained BH $f_{\rm BH} = 1$ (magenta line) and $f_{\rm BH} = 0$ (black line), respectively.

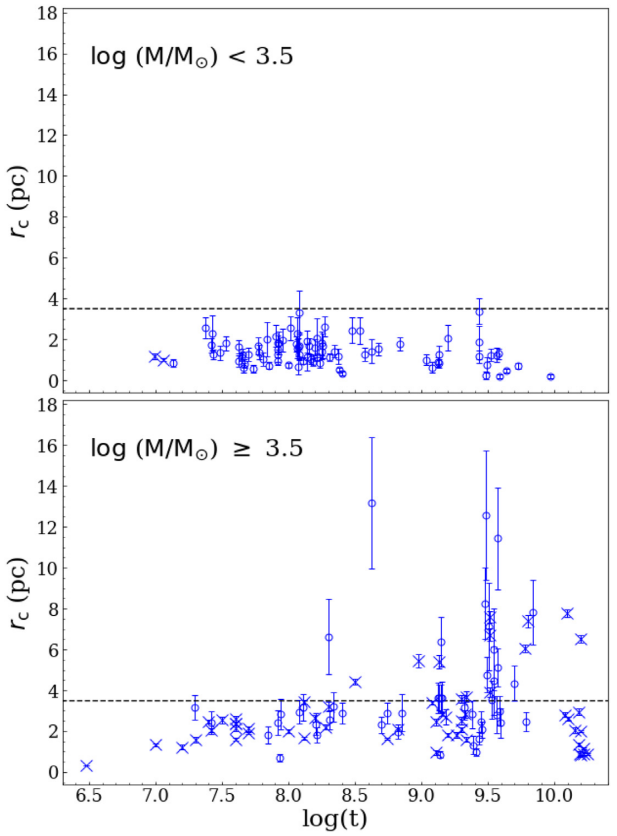

Figure 8. Same as Fig. 7 but with SCs split into different mass ranges. Top: SCs with $M < 10^{3.5}$ M$_\odot$. Bottom: SCs with $M \geq 10^{3.5}$ M$_\odot$.

bottom panel) 40 per cent of the SCs older than $\log(t) \geq 8.25$ have experienced an inner expansion. Keeping the same percentage also in the low mass interval (i.e. $M < 10^{3.5}$ M$_\odot$, top panel) we would expect to find that 13 intermediate-age SCs have $r_c \geq 3.5$ pc, while, in practice, none are observed, a result that is significant at more than the 3σ level. Another interesting feature visible in the same figure is that SCs older than 10–20 Myr in the high-mass regime seem to have, on average, a larger core radius with respect to those in the low-mass regime. This might indicate that the early expansion could be more severe for massive SCs, or perhaps that low-mass SCs that experience a great expansion do not survive. To summarize, after a rapid expansion during the first 10–20 Myr, all SCs younger than about 200–300 Myr are compact regardless of their mass, while the subsequent evolutionary path appears to be very different for low-/high-mass SCs as they get older.

In principle, we cannot exclude the possibility that only massive clusters are able to survive to old ages even if they are not very compact. However, in our sample a non-negligible number of old and low-mass SCs are present. In particular, in the low-mass regime, 18 SCs are older than 1 Gyr. This confirms our hypothesis that the SC mass is crucial to drive the core expansion.[15]

The fact that the core radius–age relationship likely originates from a physical process that begins when the SC is already a few hundred Myr old, and that affects only massive SCs, suggests that gas expulsion or mass loss due to stellar evolution are not the favourite mechanisms responsible for the expansion, as they are only effective in the early phases of a SC's life. Mackey et al. (2008) discussed the possibility that a consistent population of retained stellar mass BHs could lead to an expansion of the cluster core. Such a process starts after a few hundreds of Myr and causes a sustained increase of the cluster core, lasting for many Gyr. They tested this process through N-body simulations of massive clusters (i.e. initial total cluster masses of $\log M_{\rm tot} \sim 10^{4.75}$). By varying the fraction of retained stellar BHs at a fixed SC mass, they found that the expansion rate is strongly dependent on this fraction, and that if it is not large enough, the expansion would not begin at all. In Fig. 7, we report two runs of the N-body simulations performed by Mackey et al. (2008), extrapolated from their fig. 5. The two lines represent two extreme cases: (i) with no primordial mass segregation and a fraction of retained BH $f_{\rm BH} = 1$ and (ii) with a fraction $f_{\rm BH} = 0$. The former predicts an expansion of the core radius, which never ends, after about 1 Gyr. Mackey et al. (2008) tested also other possibilities (not displayed in the figure to preserve readability) that foresee different evolutionary paths. For example, by imposing also a primordial mass segregation, the inner expansion starts when a SC has about 10 Myr (see their fig. 15), and this occurrence might explain the few SCs younger than 1 Gyr observed to have a larger core radius. As the potential well of low-mass SCs is shallower, it would be possible that a large fraction of BHs are able to escape from their parent SC. This hypothesis might explain why we do not observe a core radius growth for low-mass SCs. Nevertheless, N-body simulations with a finer mass resolution are crucial to shed light on this matter. For example, it could clarify whether or not a small fraction of retained BHs in low-mass SCs could trigger the inner expansion.

Even the presence of an IMBH could drive a prolonged expansion of the SC radius, although Baumgardt et al. (2004b) showed that this effect is anticorrelated with the number of stars belonging to the SC, hence this outcome is at odds with our result. Nevertheless, we cannot exclude the possibility that also less massive SCs undergo an increase of their r_c, but due to their low mass (i.e. low gravitational potential) this process ends up with the evaporation of the SC. Therefore we do not observe such kind of SCs, since they dissolve faster with respect to the more massive ones.

[15]One potential selection effect is that low-mass SCs, especially with large radii (and/or old ages) are unlikely to end up in cluster catalogues in the first place.

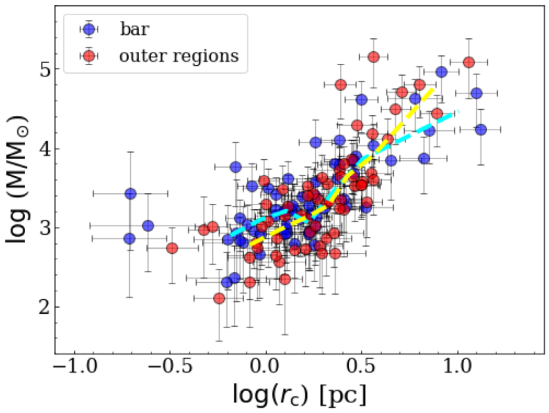

Figure 9. Mass–size relationship. The core radius was derived with an EFF profile. Blue and red points define the SCs belonging to the SMC bar and to the outer regions, respectively. Cyan and yellow dashed lines indicate the median of the SC mass calculated in bin intervals built in order to have a minimum number of 10 objects for the bar and outer SCs, respectively.

Unfortunately, all previous investigations based on *N*-body simulations studied only the evolution of SCs with $M \sim 10^4$–10^5 $M_\odot$ or larger. *N*-body studies probing lower mass SCs (down to hundreds of solar masses as in this study) are urgently needed to understand how the different physical mechanisms affect differentially low- and high-mass SCs.

6.2 Mass–radius relationship

We delved into the mass–radius relationship. Fig. 9 depicts the estimated SC mass as a function of the core radius derived through the EFF profile. We notice a tight linear trend in the log–log space along almost the whole range of core radii, even if we can recognize a few very compact but massive SCs. A weighted linear fit (i.e. $\log M = a + b \log r_c$)[16] yielded $a = 2.91 \pm 0.08$ and $b = 1.54 \pm 0.30$. We derived a Spearman rank of 0.43, with a significance larger than 99 per cent. This outcome is at odds with Mackey & Gilmore (2003b) and their sample of 10 SMC SCs, while a linear trend has been found by Carvalho et al. (2008), although their range of masses was considerably smaller than ours. In fact, it is the first time that such a trend is observed in the SMC for a conspicuous number of SCs spanning an interval of masses of ∼4 order of magnitudes, down to hundreds of solar masses.

In Fig. 9, we also analysed separately the behaviour of the SCs located within the SMC bar and in the outer regions (see also Fig. 1). An inspection of this figure suggests that the most compact objects are in the bar. Looking at the median masses that are outlined with dashed lines in Fig. 9 for both inner and outer SCs, we observed, on average, a similar mass at any given radius between the two subpopulations, indicating that the bar, despite being a denser environment, might not have a primary role in the evolutionary path of the SCs in the SMC.

6.3 SC parameters as function of their spatial positions

We investigated the distribution of the SC main parameters as a function of their galactocentric distance. Fig. 10 shows the distribution of the age (top panel), core radius (middle panel), and mass

[16]We adopted the RANdom SAmple Consensus (RANSAC) algorithm implemented by the SCIKIT-LEARN python package (Pedregosa et al. 2011), in conjunction with a bootstrap procedure.

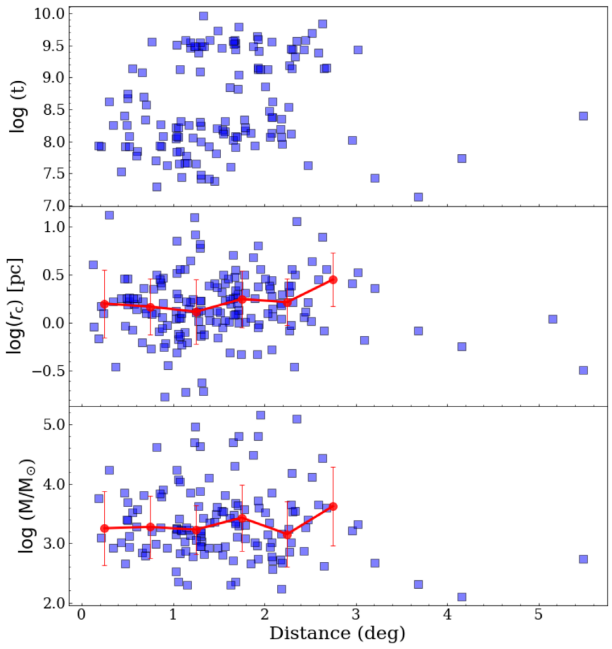

Figure 10. Age (top), core radius (middle), and mass (bottom) as a function of galactocentric distance, expressed in degrees. Red circles mark the medians estimated in bins of 0.°5.

(bottom panel) with the distance. Regarding the age, the majority of SCs younger than ∼log (*t*) = 8.5 dex are placed in the bar. Vice versa, beyond ∼1.°5 the SC population is preferentially composed of intermediate-age objects. This result is consistent with the literature (e.g. Maia et al. 2014; Dias et al. 2016; Bica et al. 2020; Piatti 2021). No apparent trend stands out clearly in the last two panels, as is evident also by the medians of these physical quantities. The SCs located beyond 3° belong to the SMC Bridge and are younger than 1 Gyr. Moreover, their size and mass are smaller than the averages estimated within 3° (i.e. ∼1 pc and ≤1000 $M_\odot$, respectively). We can speculate that this reflects their birth in a low-density region.

7 DISCUSSION

A mass–radius relation is expected to be present since the early stages of SC formation. Indeed, a relation of the form $R \propto M^\alpha$ has been found in the Milky Way (MW)'s SC-forming regions, where they are present as dense clumps within giant molecular clouds (GMCs). The same kind of relation was found very recently also in the LMC (see Mok, Chandar & Fall 2021, and references therein). The exponent of this power law estimated from the protoclusters is in the range $0.3 \leq \alpha \leq 0.6$. A mass–radius direct proportionality holds also in the already formed SCs, and it has been observed in other environments beside the MW, such as nearby galaxies (e.g. M31, M51, M82, etc., see the detailed review by Krumholz, McKee & Bland-Hawthorn 2019, and references therein). In fig. 9 of Krumholz et al. (2019), the authors drew on the same plot the half-light radius as a function of the mass for SCs belonging to many different galaxies in the Local Group, concluding that the relation seems to have the general form $r_h \propto M^{1/3}$.[17] Nevertheless, the authors also pointed out that the scatter is too broad to devise a linear fit, either by considering only SCs hosted by the same galaxy or all SCs belonging to different

[17]In this work (see also Fig. 9) we obtained a relation of $r_c \propto M^{0.34}$.

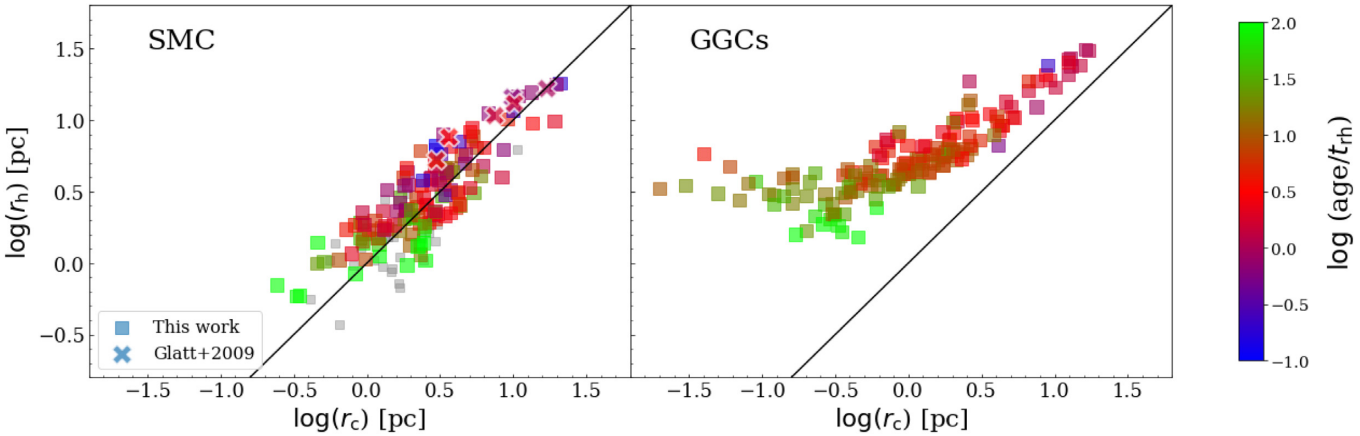

Figure 11. Left: half-light radius as a function of core radius, estimated in this work using King profiles. Right: same plot for GGCs taken from Baumgardt's GGC data base. Crosses indicate six SCs analysed by Glatt et al. (2009). The black solid line indicates the one-to-one relationship. SCs are colour coded according their dynamical age (see definition in the text). SCs with no estimated age are plotted in grey.

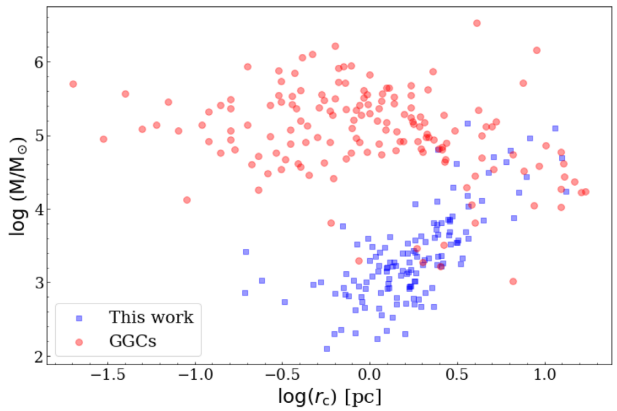

Figure 12. Core radius–mass relationship with GGCs (red points) and our SMC sample (blue points).

systems. As a cluster grows older, new physical mechanisms become dominant and the mass–radius trend could change or even reverse its sign.

We can take advantage of our large sample of SCs to investigate the dynamical status of our SCs. Mass segregation and core collapse may be signs of an advanced evolutionary phase. A good proxy for the dynamical evolutionary status of a SC is represented by the ratio between the age and the relaxation time of the SC, i.e. age/t_{rh}. According to Spitzer (1987), t_{rh} is expressed as

$$t_{rh} = 8.933 \times 10^5 \text{ yr} \times \frac{1}{\ln(0.4N_*)} \langle m_* \rangle^{-1} M^{1/2} r_h^{3/2}, \quad (4)$$

where $N_* = M/\langle m_* \rangle$ is the estimated number of stars belonging to the SC and $\langle m_* \rangle$ is the average stellar mass in solar units. To get an appropriate $\langle m_* \rangle$, we integrated IMF models of different ages, in order to derive a very tight $\langle m_* \rangle$–age relationship. Glatt et al. (2011) determined the present day mass function of six intermediate-age SMC SCs (in the age interval between 6 and 10.5 Gyr) using deep data from the *Hubble Space Telescope* (*HST*), finding that all six SCs show signs of mass segregation to different degrees, suggesting that they are dynamically evolved and/or had primordial mass segregation. They also estimated the present day relaxation time for the six SCs to be a few Gyr, i.e. comparable to their ages, with the exception of one object. In Fig. 11, we plotted the estimated half-light radius as a function of the core radius, with SCs painted with different colours according to their evolutionary age for the SMC SCs investigated in this work (left-hand panel). The six SCs studied by Glatt et al. (2011) are also overplotted in Fig. 11[18] and their dynamical ages are very similar to most SCs investigated in this work, hence we expect that also other SMC SCs might show signs of mass segregation.

In the right-hand panel of the same figure, we also plotted the GGCs.[19] The GGC population is quite different with respect to the SMC SC system, as it contains much more massive and much older objects. In particular, the SMC contains only one GC (i.e. NGC 121), while the MW does not have populous intermediate-age and young SCs as the SMC. Also, GGCs are objects typically older than 10 Gyr. Nevertheless, it would be instructive comparing the two systems. In addition, the MW is also representative of a very different environment with respect to the SMC (i.e. stronger tidal fields, the presence of a bulge and a thick and thin disc where the GGCs pass through, etc.). A remarkable feature visible in Fig. 11 for the GGCs is a noteworthy deviation from the identity relationship for $r_c \leq 5$ pc ($\log r_c \sim 0.7$). While going towards lower r_c values the trend flattens out, settling around $r_h \sim 1$–3 pc ($\log r_h \sim 0.0$–0.5) at the lowest end of the relation. As suggested by Djorgovski (1996), r_c and r_h are fairly similar as long as $t_{rc} \gg$ SC age, after which the core collapses with little changes in the half-light radius. A completely different behaviour is visible for the SMC clusters studied here. Indeed, a linear trend emerges for the entire range of observed radii. This reveals that, unlike SMC SCs, the GGCs have entered a core-collapse phase despite a similar age/t_{rh} ratio, suggesting that the SC evolutionary path in the two systems is noticeably different.

In order to better investigate how a different evolutionary status leads to different mass–size trends, in Fig. 12 we compare mass versus core radius for our sample of SCs with those of GGCs. This plot shows that, in contrast to the SMC case, the average mass of GGCs is quite constant (i.e. $\log(M/M_\odot) \sim 10^5$–$10^{5.5}$ dex) up to $r_c \leq 1$ pc, then it begins to decrease at larger core radii. As anticipated,

[18]Their sizes have been taken from Glatt et al. (2009).
[19]Here we exploited data from Baumgardt's GGC database (https://people.smp.uq.edu.au/HolgerBaumgardt/globular/) that contains an up-to-date compilation of 158 GGCs fundamental parameters.

the break of the mass–size relationship, or even the reverse sign at the upper end, reveals that the dynamical state of GGCs entered the so-called core-collapse phase (Harris 1996; McLaughlin & van der Marel 2005). Additionally, the mass spectrum of the two galaxies is remarkably different. The SCs analysed in this work cover a broad range of masses, from hundreds up to a million of solar masses, while the majority of the GGCs have $M \geq 10^4$ $M_\odot$ (e.g. Harris 1996; Baumgardt & Hilker 2018). It is evident that tidal effects of the MW had a great impact on the survival of the low-mass GGCs, as expected, while this effect is not visible in the SMC, at least in our sample. In their landmark paper, Gnedin & Ostriker (1997) investigated the destruction of the GGCs and showed that in the inner regions, only fairly massive and compact clusters can survive. This is largely due to external effects such as tides, disc shocks, etc., which should be largely absent in the SMC. Thus, environment can play a considerable role, but is probably much less important in a dwarf irregular like the SMC. Another key difference is the age: with the exception of NGC 121, the SMC SCs are much younger than the GGCs and hence had less time to evolve dynamically. To summarize, although the SMC SCs seem dynamically evolved, showing in a few cases signs of mass segregation (Glatt et al. 2011), they are not in a core-collapse phase yet.

8 CONCLUSIONS

We provide SBPs from homogeneous *g*-band integrated photometry for 170 SMC SCs. For 62 of them this is the first SBP appearing in the literature. The derived profiles were fitted with EFF and King models. We list for all the clusters the structural parameters obtained from the SBP fits (core and half-light radii, total luminosity, etc.). We estimated ages and masses for 134 SCs by means of the open source python package ASteCA. Finally, we derived the projected distances of all SCs with respect to the SMC centre to investigate if/how their properties vary with galactocentric distance. The main results of this study are the following.

(i) We find that young SCs are compact, while clusters older than $\log(t) \sim 8.3$ show a wide range of r_c values. This occurrence has been already noted and discussed in the literature, here we confirm and strengthen it on the basis of a much larger SC sample. The quoted feature has been observed also in other galaxies (see discussion in the Introduction), suggesting that the evolutionary path of SCs is the same regardless of the hosting galaxy. However, the physical mechanism responsible for this phenomenon is still unclear. We speculate that the SC mass is the main parameter driving the inner expansion, as none of the SCs with $\log(M/M_\odot) < 3.5$ dex have been observed to go through such an expansion.

(ii) A mass–size relation clearly stands out over almost the entire range of radii covered in this work. Analysing this relationship separately for SCs placed in the bar (i.e. with distance $d \leq 1.^\circ5$ from the SMC centre) and those outside, we did not find any remarkable difference.

(iii) We do not find any trend of the relevant SC parameters with distance from the SMC centre, except that young SCs are mainly concentrated in the bar and vice versa. We caution that projection effects may play a role given the large depth extent of the SMC.

(iv) We derived the dynamical age of our sample and we excluded that any of the studied SCs is in a core-collapse phase. However, we cannot rule out that some of them present mass segregation to different degrees, as observed by Glatt et al. (2011), in a subsample of six old ($t > 6$ Gyr) SMC SCs.

ACKNOWLEDGEMENTS

We thank the referee for helpful comments and suggestions that helped us to improve the paper. MG and VR acknowledge support from the INAF grant 'Funzionamento VST' (1.05.03.02.04).

This work has been partially supported by INAF through the 'Main Stream SSH program' (1.05.01.86.28).

MC acknowledges the support of INFN 'Iniziativa specifica TAsP'. We thank L. Limatola and A. Grado for their help with the data reduction.

We sincerely thank M.-R. L. Cioni for a critical reading of the paper.

This research was made possible through the use of the AAVSO Photometric All-Sky Survey (APASS), funded by the Robert Martin Ayers Sciences Fund and NSF AST-1412587.

This work is based on INAF-VST guaranteed observing time under ESO programmes: 099.D-0673(A); 098.D-0579(A); 097.D-0209(A); 096.D-0535(A); 095.D-0132(A); 094.D-0492(A); 093.D-0174(A); 092.D-0214(A); 091.D-0574(A); 090.D-0172(A); 089.D-0258(A); and 088.D-4014(A).

DATA AVAILABILITY

The data underlying this paper are available in the paper and in its online supplementary material.

REFERENCES

Banerjee S., Kroupa P., 2017, A&A, 597, A28
Bastian N., Gieles M., Goodwin S. P., Trancho G., Smith L. J., Konstantopoulos I., Efremov Y., 2008, MNRAS, 389, 223
Bastian N. et al., 2012, MNRAS, 419, 2606
Baumgardt H., Hilker M., 2018, MNRAS, 478, 1520
Baumgardt H., Kroupa P., 2007, MNRAS, 380, 1589
Baumgardt H., Makino J., Ebisuzaki T., 2004a, ApJ, 613, 1133
Baumgardt H., Makino J., Ebisuzaki T., 2004b, ApJ, 613, 1143
Bica E., Bonatto C., Dutra C. M., Santos J. F., 2008, MNRAS, 389, 678
Bica E. et al., 2020, AJ, 159, 82
Bradley L. et al., 2019, astropy/photutils: v0.7.2. Zenodo, Available at:https://doi.org/10.5281/zenodo.3568287
Bressan A., Marigo P., Girardi L., Salasnich B., Dal Cero C., Rubele S., Nanni A., 2012, MNRAS, 427, 127
Carvalho L., Saurin T. A., Bica E., Bonatto C., Schmidt A. A., 2008, A&A, 485, 71
Chandar R., Whitmore B. C., Dinino D., Kennicutt R. C., Chien L. H., Schinnerer E., Meidt S., 2016, ApJ, 824, 71
Chiosi E., Vallenari A., Held E. V., Rizzi L., Moretti A., 2006, A&A, 452, 179
Dias B., Kerber L. O., Barbuy B., Santiago B., Ortolani S., Balbinot E., 2014, A&A, 561, A106
Dias B., Kerber L., Barbuy B., Bica E., Ortolani S., 2016, A&A, 591, A11
Djorgovski S., 1988, in Grindlay J. E., Philip A. G. D., eds, Proc. IAU Symp. 126, The Harlow-Shapley Symposium on Globular Cluster Systems in Galaxies. Kluwer, Dordrecht, p. 333
Djorgovski S. G., 1996, in Hut P., Makino J., eds, Proc. IAU Symp. 174, Dynamical Evolution of Star Clusters: Confrontation of Theory and Observations. Kluwer, Dordrecht, p. 9
Elson R. A. W., 1991, ApJS, 76, 185
Elson R. A. W., 1992, MNRAS, 256, 515
Elson R. A. W., Fall S. M., Freeman K. C., 1987, ApJ, 323, 54
Elson R. A. W., Freeman K. C., Lauer T. R., 1989, ApJ, 347, L69
Fouesneau M., Lançon A., 2010, A&A, 521, A22
Fouesneau M. et al., 2014, ApJ, 786, 117
Gatto M. et al., 2020, MNRAS, 499, 4114
Glatt K. et al., 2009, AJ, 138, 1403

Glatt K., Grebel E. K., Koch A., 2010, A&A, 517, A50
Glatt K. et al., 2011, AJ, 142, 36
Gnedin O. Y., Ostriker J. P., 1997, ApJ, 474, 223
Gonidakis I., Livanou E., Kontizas E., Klein U., Kontizas M., Belcheva M., Tsalmantza P., Karampelas A., 2009, A&A, 496, 375
Goodwin S. P., Bastian N., 2006, MNRAS, 373, 752
Graczyk D. et al., 2020, ApJ, 904, 13
Grado A., Capaccioli M., Limatola L., Getman F., 2012, Mem. Soc. Astron. Ital. Suppl., 19, 362
Harris W. E., 1996, AJ, 112, 1487
Haschke R., Grebel E. K., Duffau S., 2012, AJ, 144, 107
Hill A., Zaritsky D., 2006, AJ, 131, 414(HZ06)
Ivanov V. D., Piatti A. E., Beamín J.-C., Minniti D., Borissova J., Kurtev R., Hempel M., Saito R. K., 2017, A&A, 600, A112
Jacyszyn-Dobrzeniecka A. M. et al., 2016, Acta Astron., 66, 149
King I., 1962, AJ, 67, 471
Kroupa P., 2001, MNRAS, 322, 231
Kroupa P., Aarseth S., Hurley J., 2001, MNRAS, 321, 699
Krumholz M. R., Fumagalli M., da Silva R. L., Rendahl T., Parra J., 2015, MNRAS, 452, 1447
Krumholz M. R., McKee C. F., Bland-Hawthorn J., 2019, ARA&A, 57, 227
Mackey A. D., Gilmore G. F., 2003a, MNRAS, 338, 85
Mackey A. D., Gilmore G. F., 2003b, MNRAS, 338, 120
Mackey A. D., Wilkinson M. I., Davies M. B., Gilmore G. F., 2007, MNRAS, 379, L40
Mackey A. D., Wilkinson M. I., Davies M. B., Gilmore G. F., 2008, MNRAS, 386, 65
McLaughlin D. E., van der Marel R. P., 2005, ApJS, 161, 304
Maia F. F. S., Piatti A. E., Santos J. F. C., 2014, MNRAS, 437, 2005
Maia F. F. S. et al., 2019, MNRAS, 484, 5702
Merritt D., Piatek S., Portegies Zwart S., Hemsendorf M., 2004, ApJ, 608, L25
Mok A., Chandar R., Fall S. M., 2021, ApJ, 911, 8
Nayak P. K., Subramaniam A., Choudhury S., Sagar R., 2018, A&A, 616, A187
Nidever D. L. et al., 2017, AJ, 154, 199
Parisi M. C., Geisler D., Clariá J. J., Villanova S., Marcionni N., Sarajedini A., Grocholski A. J., 2015, AJ, 149, 154
Pedregosa F. et al., 2011, J. Machine Learning Res., 12, 2825
Perren G. I., Vázquez R. A., Piatti A. E., 2015, A&A, 576, A6
Perren G. I., Piatti A. E., Vázquez R. A., 2017, A&A, 602, A89
Piatti A. E., 2021, A&A, 647, A11
Piatti A. E., Bica E., 2012, MNRAS, 425, 3085
Piatti A. E., Santos J. F. C. J., Clariá J. J., Bica E., Ahumada A. V., Parisi M. C., 2005, A&A, 440, 111
Piatti A. E. et al., 2014, A&A, 570, A74
Piatti A. E., de Grijs R., Rubele S., Cioni M. R. L., Ripepi V., Kerber L., 2015, MNRAS, 450, 552
Piatti A. E., Ivanov V. D., Rubele S., Marconi M., Ripepi V., Cioni M. R. L., Oliveira J. M., Bekki K., 2016, MNRAS, 460, 383
Ripepi V. et al., 2014, MNRAS, 442, 1897
Ripepi V. et al., 2017, MNRAS, 472, 808
Roediger J. C., Courteau S., 2015, MNRAS, 452, 3209
Ryon J. E. et al., 2015, MNRAS, 452, 525
Ryon J. E. et al., 2017, ApJ, 841, 92
San Roman I., Sarajedini A., Holtzman J. A., Garnett D. R., 2012, MNRAS, 426, 2427
Santos J. F. C., Jr et al., 2020, MNRAS, 498, 205
Schlafly E F., Finkbeiner D. P., 2011, ApJ, 737, 103
Schlegel D. J., Finkbeiner D. P., Davis M., 1998, ApJ, 500, 525
Silva-Villa E., Larsen S. S., 2011, A&A, 529, A25
Song Y.-Y., Mateo M., Bailey J. I., III, Walker M. G., Roederer I. U., Olszewski E. W., Reiter M., Kremin A., 2021, MNRAS, 504, 4160
Spitzer L., 1987, Dynamical Evolution of Globular Clusters. Princeton Univ. Press, Princeton, NJ
Stetson P. B., 1987, PASP, 99, 191
Stetson P. B., 1992, in Worrall D. M., Biemesderfer C., Barnes J., eds, ASP Conf. Ser. Vol. 25, Astronomical Data Analysis Software and Systems I. Astron. Soc. Pac., San Francisco, p. 297
Subramanian S., Subramaniam A., 2012, ApJ, 744, 128
Werchan F., Zaritsky D., 2011, AJ, 142, 48
Zaritsky D., Harris J., Thompson I., 1997, AJ, 114, 1002

SUPPORTING INFORMATION

Supplementary data are available at *MNRAS* online.

Figure D1. SBPs derived as described in Section 3.

Please note: Oxford University Press is not responsible for the content or functionality of any supporting materials supplied by the authors. Any queries (other than missing material) should be directed to the corresponding author for the paper.

APPENDIX A: KING MODEL

The empirical King's profile (King 1962), expressed in mag arcsec^{-2}, is given by

$$\mu(r) = \mu' - 5\log_{10}\left(\frac{1}{\sqrt{1+\left(\frac{r}{r_c}\right)^2}} - \frac{1}{\sqrt{1+\left(\frac{r_t}{r_c}\right)^2}}\right), \quad \text{(A1)}$$

$$\mu' = \mu_0 + 5\log_{10}\left(1 - \frac{1}{\sqrt{1+\left(\frac{r_t}{r_c}\right)^2}}\right), \quad \text{(A2)}$$

where μ_0 is the central SB, r_c is the core radius, and r_t is the tidal radius. With these values, it is possible to calculate the SC concentration, defined as $c = \log(r_t/r_c)$. It is worth to point out that r_c defined through equation (A1) is similar (it indicates the distance at which the SB is half the central value) to r_c derived by means of equation (1) only if $r_t \gg r_c$ (high concentration). For low concentrations, the r_c value obtained from the King profile is larger than its counterpart determined from the EFF function (see also fig. 10 in Glatt et al. 2009).

Another useful parameter is the half-light radius (r_h), which is the radius enclosing half of the cluster total light. We derived it from the best model achieved through equation (1). We calculated the projected luminosity as a function of radius (substantially the growth curve), normalized by the total projected luminosity. The total projected luminosity is obtained by integrating up to the fitting radius. The errors are calculated with a Monte Carlo-like approach, perturbing each parameter with Gaussians with the best-fitting value as mean, and the error on the parameter as σ, and these are 'propagated' in the calculation.

Regarding the fitting procedure, and the choice of r_f for the King's profiles, we proceeded as discussed in the previous section for the EFF models.

Again, an integration of the equation (A1) by using as extreme values of the integral 0 and r_t provides the total luminosity L of the SC:

$$L = \pi r_c^2 k \left\{ \ln\left[1+\left(\frac{r_t}{r_c}\right)^2\right] + \frac{\left(\frac{r_t}{r_c}\right)^2 + 4\sqrt{1+\left(\frac{r_t}{r_c}\right)^2} - 4\left[1+\left(\frac{r_t}{r_c}\right)^2\right]}{1+\left(\frac{r_t}{r_c}\right)^2} \right\}, \quad \text{(A3)}$$

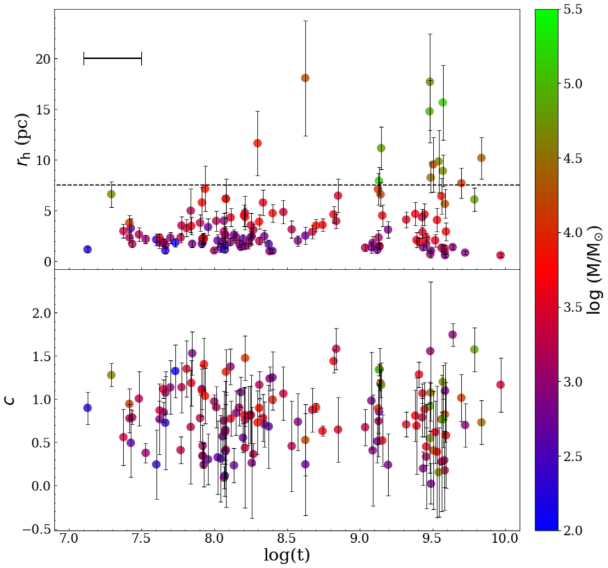

Figure A1. Top: half-light radius. Bottom: concentration parameter as a function of the SC age. Points are colour coded according their mass. Diamonds are SCs flagged as OLD (see text for details). In the lower right-hand corner of the bottom panel, we sketched the size of the age uncertainties, equal for all SCs.

$$k = 10^{-0.4\mu}\left(1 - \frac{1}{\sqrt{1+\left(\frac{r_t}{r_c}\right)^2}}\right). \quad \text{(A4)}$$

In Table C1, we reported the values of μ_0, r_c, and r_t (in arcsec), from fitting all SCs in our sample with King models. We listed luminosities, $r_c - r_h$ (in pc), and the concentration parameter in Table 1.

We also briefly discuss the parameters derived through the King profile in order to show that they provide the same results achieved with the EFF model. In Fig. A1, we display the half-light radius as a function of the age (top panel). Overall, r_h seems to show a trend with the SC age akin that observed in Fig. 7. In particular, all SCs younger than 100–300 Myr have $r_h \leq 7.5$ pc. Then, some SCs undergo an increase of their inner regions while the majority remains compact. We find also in this case that the bulk of the SCs having large half-light radius are also the most massive. Fig. A1 (bottom panel) shows the concentration parameter as a function of the age. No particular trend can be detected in this case.

APPENDIX B: DEPROJECTED DISTANCE FROM THE SMC CENTRE

To obtain the 2D distance from the SMC centre we followed the recipe developed by Piatti et al. (2005) and successively used in other works (e.g. Dias et al. 2014, 2016). The core idea is to define the distance from the SMC through ellipses, as they better reproduce the SMC 2D geometry. Following Piatti et al. (2005), we draw ellipses with an ellipticity of $e = 0.5$, having the semimajor axis direction at 45°, starting from the north in a counterclockwise pattern. For each SC, we looked for the ellipse intersecting its position and we set the major axis of the ellipse as the SC galactocentric distance. Moreover, following Dias et al. (2016) we also split our SC sample into subpopulations based on their 2D distance: (i) the bar, constituted by SCs with a distance lower than 1°.5 and (ii) the outer regions, made by the remaining objects. Note that while Dias et al. (2016) called bar those SCs within 2°, we utilized a separation of 1°.5 in order to have a similar number of SCs in each of the two subpopulations.

APPENDIX C: PARAMETERS OF THE FITTING PROCEDURE

In Table C1, we reported all the SC parameters derived by fitting the SBPs with EFF and King profiles. In the first column the SC's name is displayed, while in the second and third columns SCs' coordinates are reported. From the fourth to the sixth columns we inserted fitting parameters estimated through the EFF profile, namely μ_0, α, and γ that are described in Section 4.1. From the seventh to the ninth columns we put parameters obtained via the King profile, or μ_0, r_c, and r_t, described in Appendix A. The last two columns display the fitting radius (see discussion in Section 4.1) and the tile where SCs reside.

Table C1. Parameters derived by fitting the EFF and King profiles.

ID			EFF			King				
	RA (J2000)	Dec. (J2000)	μ_0 (mag arcsec^{-2})	α (arcsec)	γ	μ_0 (mag arcsec^{-2})	r_c (arcsec)	r_t (arcsec)	r_f (arcsec)	Tile
B10	9.4345	− 73.2108	16.78 ± 1.33	1.0 ± 0.8	2.8 ± 0.6	17.19 ± 1.68	0.8 ± 0.8	28.8 ± 25.8	12.0	3_4
B100	15.0999	− 72.0888	17.96 ± 0.10	4.0 ± 0.4	4.5 ± 0.4	17.79 ± 0.16	2.1 ± 0.2	19.9 ± 1.2	16.0	4_6
B103	15.2375	− 73.1541	20.02 ± 0.21	2.9 ± 1.0	2.0 ± 0.4	20.24 ± 0.24	4.5 ± 1.4	28.8 ± 13.4	16.0	3_5
B105	15.4037	− 72.4073	19.41 ± 0.23	3.0 ± 0.9	2.4 ± 0.4	19.49 ± 0.19	3.1 ± 0.6	37.3 ± 14.2	16.0	4_6
B108	15.4637	− 72.1821	21.39 ± 0.23	4.3 ± 2.6	2.0 ± 1.0	21.51 ± 0.23	6.5 ± 3.0	31.7 ± 26.0	16.0	4_6
B111	15.5094	− 71.0208	21.78 ± 0.18	2.7 ± 0.9	2.0 ± 0.5	21.95 ± 0.19	3.9 ± 1.1	28.1 ± 16.2	12.0	5_6
B113	15.7273	− 73.3380	20.25 ± 0.22	5.1 ± 2.3	3.9 ± 1.7	20.25 ± 0.20	4.0 ± 1.0	18.8 ± 4.4	12.0	3_6
B115	15.8500	− 72.6516	19.35 ± 0.27	3.4 ± 1.8	2.0 ± 0.7	19.57 ± 0.27	5.4 ± 2.5	33.6 ± 30.1	16.0	4_6
B117	16.0545	− 73.2603	19.64 ± 0.12	4.0 ± 0.9	2.5 ± 0.4	19.69 ± 0.13	4.1 ± 0.7	33.0 ± 10.2	16.0	3_6
B119	16.0813	− 73.1678	–	–	–	21.96 ± 0.19	9.7 ± 7.7	12.3 ± 2.9	10.0	3_6
B12	9.5871	− 73.2707	–	–	–	21.96 ± 0.24	8.0 ± 6.5	17.4 ± 10.1	13.0	3_4
B121	16.1257	− 72.6191	19.45 ± 0.21	5.3 ± 2.6	2.8 ± 1.3	19.65 ± 0.11	8.7 ± 2.0	19.3 ± 2.0	16.0	4_6
B122	16.1007	− 71.7144	21.92 ± 0.35	6.8 ± 5.4	2.0 ± 1.1	22.47 ± 0.18	20.5 ± 15.1	56.1 ± 48.3	32.0	5_6
B124	16.2608	− 73.0427	20.57 ± 0.13	6.5 ± 2.5	4.2 ± 1.8	20.66 ± 0.11	6.7 ± 1.5	16.8 ± 2.2	13.0	3_6
B128	16.4628	− 71.9534	–	–	–	21.45 ± 0.26	9.6 ± 6.2	20.4 ± 6.9	16.0	4_6
B137	17.6174	− 72.9574	20.18 ± 0.12	2.8 ± 0.5	2.0 ± 0.2	20.35 ± 0.16	3.8 ± 0.8	38.8 ± 18.6	16.0	3_6
B165	22.7115	− 73.4340	21.46 ± 0.25	6.3 ± 2.5	4.8 ± 1.9	21.55 ± 0.23	5.0 ± 1.2	18.3 ± 1.8	16.0	3_8
B18	10.2765	− 72.7259	20.35 ± 0.14	3.4 ± 1.2	3.6 ± 1.4	20.34 ± 0.13	2.7 ± 0.6	13.7 ± 4.9	6.0	4_4
B21	10.3142	− 72.8316	21.29 ± 0.41	2.8 ± 2.7	2.3 ± 2.0	21.53 ± 0.11	8.2 ± 3.7	8.6 ± 0.7	8.0	4_4
B22	10.3361	− 72.8244	18.32 ± 0.66	0.7 ± 0.3	2.0 ± 0.2	18.96 ± 0.39	1.1 ± 0.3	15.9 ± 6.8	6.0	4_4
B26	10.1890	− 73.7390	21.23 ± 0.29	2.4 ± 1.5	2.6 ± 1.4	21.51 ± 0.10	4.8 ± 1.3	8.2 ± 0.9	6.0	3_4
B34A	11.1054	− 72.9446	19.50 ± 0.43	5.0 ± 4.0	5.4 ± 4.8	19.77 ± 0.31	5.6 ± 2.7	10.5 ± 1.3	10.0	3_4
B39	11.3626	− 73.4800	20.49 ± 0.09	5.1 ± 1.0	2.0 ± 0.3	20.61 ± 0.12	7.1 ± 1.4	53.8 ± 21.2	25.0	3_4
B52	12.4189	− 73.0582	21.41 ± 0.16	13.5 ± 8.8	2.0 ± 1.2	21.65 ± 0.12	35.0 ± 25.9	62.5 ± 33.4	40.0	3_5
B65	13.1845	− 72.9795	17.93 ± 0.08	8.6 ± 1.4	6.6 ± 1.3	17.88 ± 0.10	4.6 ± 0.5	20.0 ± 1.3	16.0	3_5
B70	13.3609	− 71.7489	19.68 ± 0.11	1.7 ± 0.2	2.2 ± 0.1	19.64 ± 0.10	1.5 ± 0.1	84.2 ± 20.0	20.0	5_5
B71	13.3237	− 72.7660	18.63 ± 0.13	13.2 ± 4.9	7.5 ± 3.7	18.71 ± 0.12	9.4 ± 1.8	22.4 ± 1.5	20.0	4_5
B79	13.6992	− 72.4661	18.73 ± 0.20	5.3 ± 1.7	2.8 ± 0.6	18.69 ± 0.21	4.2 ± 0.9	57.7 ± 28.3	25.0	4_5
B80	13.7084	− 73.2241	20.13 ± 0.40	2.1 ± 1.2	2.0 ± 0.6	20.39 ± 0.34	3.1 ± 1.3	29.8 ± 26.4	12.0	3_5
B9	9.3155	− 72.9626	20.97 ± 0.42	3.7 ± 3.0	2.3 ± 1.3	21.30 ± 0.20	8.8 ± 3.4	17.8 ± 2.2	16.0	4_4
B96	14.8078	− 72.6089	20.75 ± 0.08	16.7 ± 5.7	5.8 ± 2.7	20.79 ± 0.07	13.7 ± 2.5	31.7 ± 3.2	25.0	4_6
B97	14.9158	− 71.7446	21.87 ± 0.26	4.5 ± 3.9	2.0 ± 1.6	22.08 ± 0.16	10.1 ± 6.8	18.9 ± 8.6	12.0	5_6
B99	15.1180	− 73.0865	20.21 ± 0.20	5.3 ± 2.3	2.4 ± 0.8	20.27 ± 0.19	6.0 ± 1.7	39.8 ± 19.4	20.0	3_5
BS 102	15.3120	− 73.7949	21.64 ± 0.22	4.2 ± 2.5	2.2 ± 1.2	21.74 ± 0.18	5.5 ± 2.1	26.4 ± 18.9	12.0	3_6
BS 128	16.3894	− 73.4904	–	–	–	21.29 ± 0.22	3.5 ± 2.2	23.3 ± 54.7	6.0	3_6
BS 131	16.4978	− 72.3411	19.70 ± 0.14	5.6 ± 3.3	3.1 ± 2.2	19.79 ± 0.12	7.7 ± 3.4	14.9 ± 4.3	10.0	4_6
BS 138	16.8159	− 72.1005	22.30 ± 0.12	11.7 ± 8.5	2.0 ± 1.6	22.38 ± 0.13	19.8 ± 15.5	48.7 ± 47.6	25.0	4_6
BS 2	7.1291	− 73.0137	21.86 ± 0.26	5.0 ± 2.3	3.6 ± 1.4	21.82 ± 0.29	3.5 ± 1.1	29.9 ± 14.7	16.0	3_3
BS 276	17.5233	− 72.7370	17.63 ± 0.18	2.3 ± 0.4	3.1 ± 0.3	17.47 ± 0.26	1.5 ± 0.3	26.0 ± 3.8	16.0	4_6
BS 76	13.9092	− 71.9203	20.97 ± 0.12	7.7 ± 2.4	3.3 ± 1.0	20.96 ± 0.12	6.2 ± 1.2	42.7 ± 16.8	20.0	5_6
BS 88	14.4583	− 72.9444	21.69 ± 0.17	4.1 ± 3.4	2.0 ± 1.8	21.79 ± 0.11	7.6 ± 5.4	14.4 ± 9.0	8.0	4_6
H86−11	8.2348	− 73.5038	20.48 ± 0.58	1.6 ± 1.1	2.0 ± 0.6	21.00 ± 0.44	3.0 ± 1.5	23.0 ± 16.8	12.0	3_3
H86−114	12.6414	− 72.6520	20.08 ± 0.12	4.7 ± 1.3	2.0 ± 0.4	20.22 ± 0.13	7.2 ± 1.7	37.1 ± 13.5	20.0	4_5
H86−137	13.1392	− 72.6804	19.85 ± 0.06	3.0 ± 0.3	2.2 ± 0.2	19.86 ± 0.06	3.0 ± 0.2	65.3 ± 32.2	12.0	4_5
H86−146	13.4132	− 72.3935	17.61 ± 0.65	1.2 ± 0.7	2.0 ± 0.3	18.16 ± 0.56	2.0 ± 0.8	41.3 ± 25.4	20.0	4_5
H86−150	13.7475	− 73.4191	19.83 ± 0.23	3.1 ± 1.3	2.0 ± 0.5	20.06 ± 0.25	5.0 ± 1.9	29.4 ± 16.7	16.0	3_5
H86−159	13.7995	− 72.6830	21.15 ± 0.17	7.8 ± 4.1	3.7 ± 2.2	21.17 ± 0.17	6.6 ± 2.2	27.7 ± 12.1	16.0	4_5
H86−165	13.9242	− 72.8798	21.07 ± 0.27	5.7 ± 4.3	2.1 ± 1.3	21.16 ± 0.25	8.3 ± 4.4	36.6 ± 28.0	20.0	4_5
H86−174	14.3251	− 72.9343	20.63 ± 0.16	4.3 ± 1.6	2.1 ± 0.6	20.74 ± 0.15	5.9 ± 1.6	32.3 ± 15.6	16.0	4_6
H86−175	14.4596	− 72.4401	19.57 ± 0.09	9.2 ± 3.6	14.4 ± 9.0	19.56 ± 0.10	4.2 ± 0.6	9.6 ± 0.5	8.0	4_6
H86−179	14.4882	− 72.4456	20.72 ± 0.42	4.8 ± 4.7	2.9 ± 2.6	20.95 ± 0.28	8.7 ± 6.0	15.3 ± 4.0	12.0	4_6
H86−181	14.5811	− 72.2996	17.97 ± 0.35	1.8 ± 0.7	2.4 ± 0.4	18.05 ± 0.35	1.8 ± 0.5	27.3 ± 12.2	12.0	4_6
H86−182	14.6073	− 72.6656	20.42 ± 0.16	9.2 ± 4.4	2.7 ± 1.3	20.48 ± 0.15	10.2 ± 3.3	44.7 ± 20.1	25.0	4_6
H86−186	14.9814	− 72.3719	19.11 ± 0.06	6.2 ± 0.7	4.7 ± 0.5	19.06 ± 0.08	3.9 ± 0.4	22.5 ± 1.7	16.0	4_6
H86−190	15.1377	− 72.2581	19.50 ± 0.32	2.1 ± 1.2	2.0 ± 0.8	19.72 ± 0.26	3.2 ± 1.4	17.1 ± 13.6	8.0	4_6
H86−191	15.2430	− 72.5398	–	–	–	21.03 ± 0.30	6.5 ± 4.9	13.3 ± 5.3	10.0	4_6
H86−193	15.3260	− 72.2283	21.35 ± 0.08	8.4 ± 3.7	3.5 ± 2.0	21.36 ± 0.08	7.6 ± 2.0	28.0 ± 13.4	12.0	4_6
H86−194	15.3105	− 72.5506	20.25 ± 0.54	2.3 ± 2.2	2.0 ± 1.4	20.74 ± 0.11	7.7 ± 3.2	10.0 ± 1.4	8.0	4_6
H86−213	23.6721	− 73.2746	20.22 ± 0.36	1.1 ± 0.3	2.0 ± 0.2	20.68 ± 0.32	1.7 ± 0.4	29.7 ± 12.9	12.0	3_8
H86−6	7.3467	− 72.9988	22.25 ± 0.19	6.2 ± 3.5	4.3 ± 2.9	22.42 ± 0.11	8.0 ± 2.6	12.7 ± 1.5	10.0	3_3
H86−60	10.1858	− 73.1180	–	–	–	21.34 ± 0.24	4.9 ± 3.7	9.2 ± 4.0	6.0	3_4
H86−74	11.3058	− 73.2199	18.31 ± 0.12	3.5 ± 0.7	2.4 ± 0.3	18.34 ± 0.12	3.4 ± 0.5	44.4 ± 17.9	16.0	3_4

Table C1 – *continued*

ID			EFF			King				
	RA (J2000)	Dec. (J2000)	μ_0 (mag arcsec^{-2})	α (arcsec)	γ	μ_0 (mag arcsec^{-2})	r_c (arcsec)	r_t (arcsec)	r_f (arcsec)	Tile
H86−86	11.7602	−73.3945	20.27 ± 0.42	1.4 ± 0.7	2.8 ± 0.9	20.34 ± 0.41	1.4 ± 0.5	10.8 ± 5.2	5.0	3_4
H86−87	11.7713	−73.3706	21.07 ± 0.23	5.6 ± 4.4	2.0 ± 1.5	21.34 ± 0.15	13.4 ± 11.2	24.5 ± 15.8	16.0	3_4
H86−97	11.9695	−73.2217	19.64 ± 0.13	5.0 ± 2.0	2.0 ± 0.7	19.80 ± 0.09	8.9 ± 2.4	25.8 ± 7.5	16.0	3_4
HW 10	9.1296	−72.9866	22.23 ± 0.12	9.9 ± 3.0	2.0 ± 0.4	22.34 ± 0.15	14.5 ± 3.8	96.4 ± 45.7	50.0	3_4
HW 11	9.3803	−73.6131	21.78 ± 0.23	11.9 ± 6.9	2.0 ± 0.8	21.91 ± 0.24	17.7 ± 7.6	126.4 ± 107.4	64.0	3_4
HW 14	10.0640	−73.8710	23.00 ± 0.14	23.6 ± 16.8	2.0 ± 1.5	23.13 ± 0.13	44.7 ± 32.0	114.3 ± 97.1	60.0	3_4
HW 18	10.7491	−72.4121	21.07 ± 0.24	1.6 ± 0.5	2.0 ± 0.4	21.42 ± 0.25	2.7 ± 0.9	15.6 ± 7.2	8.0	4_4
HW 22	11.6878	−72.0632	19.74 ± 0.10	4.0 ± 0.5	2.8 ± 0.2	19.66 ± 0.13	3.0 ± 0.3	57.3 ± 12.8	25.0	4_5
HW 26	12.3886	−73.7053	15.17 ± 0.39	0.8 ± 0.1	3.2 ± 0.2	–	–	–	8.0	3_5
HW 34	14.4662	−73.5455	–	–	–	21.37 ± 0.15	6.2 ± 4.3	9.3 ± 3.2	6.0	3_5
HW 35	14.6820	−73.5834	20.60 ± 0.08	3.6 ± 0.6	2.7 ± 0.3	20.58 ± 0.08	3.0 ± 0.3	36.7 ± 10.9	12.0	3_5
HW 36	14.7667	−73.8414	20.95 ± 0.27	5.6 ± 3.1	5.5 ± 3.6	21.00 ± 0.29	4.0 ± 1.5	13.1 ± 2.7	10.0	3_5
HW 37	13.8725	−71.8852	–	–	–	19.96 ± 0.42	11.3 ± 8.7	19.8 ± 3.0	20.0	5_6
HW 38	14.8576	−73.8170	22.45 ± 0.18	9.8 ± 7.6	2.7 ± 2.4	22.48 ± 0.18	10.8 ± 5.7	41.0 ± 36.0	20.0	3_5
HW 40	15.1060	−71.2949	21.50 ± 0.08	7.1 ± 0.9	3.0 ± 0.3	21.47 ± 0.08	5.5 ± 0.5	64.1 ± 10.6	32.0	5_6
HW 41	15.1485	−71.4601	22.45 ± 0.21	9.3 ± 4.6	2.0 ± 0.7	22.80 ± 0.17	18.4 ± 7.1	107.1 ± 86.5	50.0	5_6
HW 43	15.2849	−71.7537	21.10 ± 0.16	5.4 ± 2.3	2.0 ± 0.7	21.22 ± 0.15	8.5 ± 2.7	35.3 ± 15.0	20.0	5_6
HW 44	15.3429	−73.7883	21.45 ± 0.30	4.7 ± 3.7	2.0 ± 1.3	21.91 ± 0.14	14.3 ± 11.4	25.3 ± 14.3	16.0	3_6
HW 48	16.2437	−73.6375	19.85 ± 0.10	3.7 ± 0.5	2.5 ± 0.2	19.80 ± 0.11	3.1 ± 0.3	72.9 ± 27.3	20.0	3_6
HW 50	16.5115	−71.7110	21.72 ± 0.53	3.7 ± 3.4	2.0 ± 1.1	–	–	–	20.0	5_6
HW 52	16.7359	−73.2362	20.88 ± 0.18	8.1 ± 4.6	3.0 ± 1.7	21.03 ± 0.11	14.0 ± 4.7	24.1 ± 3.0	20.0	3_6
HW 53	16.7452	−73.5779	21.99 ± 0.08	5.5 ± 2.9	2.9 ± 2.0	22.04 ± 0.07	7.3 ± 2.8	14.3 ± 4.9	8.0	3_6
HW 54	16.8157	−72.1007	21.94 ± 0.30	6.2 ± 4.9	2.0 ± 1.2	–	–	–	25.0	4_6
HW 55	16.8292	−73.3783	22.17 ± 0.17	6.9 ± 4.2	2.0 ± 1.1	22.42 ± 0.08	17.6 ± 8.7	30.7 ± 10.2	20.0	3_6
HW 59	17.2230	−73.2419	–	–	–	20.03 ± 0.23	2.1 ± 0.6	3.3 ± 0.1	3.0	3_6
HW 61	17.4270	−72.2952	21.02 ± 0.19	6.5 ± 4.7	2.3 ± 1.7	21.11 ± 0.10	12.2 ± 4.7	21.3 ± 4.2	16.0	4_6
HW 68	18.4701	−73.4165	21.19 ± 0.46	2.2 ± 1.5	2.0 ± 0.8	21.62 ± 0.39	4.1 ± 2.4	24.4 ± 22.2	12.0	3_6
HW 74	19.2002	−73.1601	22.02 ± 0.24	8.4 ± 6.5	2.3 ± 1.7	22.10 ± 0.19	12.3 ± 5.7	38.5 ± 17.0	25.0	3_7
HW 78	20.3360	−73.0942	19.49 ± 0.24	4.7 ± 1.4	4.8 ± 1.2	19.41 ± 0.34	2.6 ± 0.7	20.2 ± 3.2	16.0	3_7
HW 8	8.4446	−73.6333	19.51 ± 0.28	3.4 ± 1.1	2.0 ± 0.3	19.66 ± 0.31	4.5 ± 1.2	100.9 ± 48.6	50.0	3_3
HW 82	21.1158	−73.1707	19.25 ± 0.30	1.9 ± 0.6	2.0 ± 0.2	19.56 ± 0.29	2.7 ± 0.6	57.1 ± 26.5	25.0	3_7
HW 9	9.1051	−73.0011	22.03 ± 0.15	4.0 ± 1.4	2.0 ± 0.5	22.22 ± 0.17	6.8 ± 2.4	28.1 ± 13.3	16.0	3_4
IC 1611	14.9513	−72.3340	18.73 ± 0.09	6.5 ± 1.0	2.3 ± 0.2	18.73 ± 0.10	6.2 ± 0.6	184.5 ± 89.8	50.0	4_6
IC 1612	15.0079	−72.3700	20.74 ± 0.18	11.0 ± 6.6	2.0 ± 1.0	21.07 ± 0.14	28.0 ± 19.4	72.7 ± 61.1	40.0	4_6
IC 1624	16.3380	−72.0434	19.23 ± 0.06	12.1 ± 1.5	3.5 ± 0.4	19.21 ± 0.07	8.9 ± 0.8	70.1 ± 9.2	40.0	4_6
IC 1662	18.1363	−73.4569	20.88 ± 0.15	11.8 ± 3.8	3.4 ± 1.0	20.87 ± 0.16	9.0 ± 1.9	72.7 ± 24.9	40.0	3_6
K1	5.3578	−73.7486	22.65 ± 0.08	38.3 ± 12.7	3.7 ± 1.4	22.65 ± 0.08	29.9 ± 6.0	160.6 ± 61.5	80.0	3_3
K11	9.1131	−72.4786	22.06 ± 0.10	18.6 ± 4.9	5.0 ± 1.5	22.03 ± 0.11	11.5 ± 1.9	58.6 ± 9.8	40.0	4_4
K13	8.9196	−73.5981	22.60 ± 0.17	19.9 ± 14.0	2.0 ± 1.3	22.84 ± 0.10	63.1 ± 50.0	90.0 ± 35.5	64.0	3_4
K15	10.0556	−72.6988	20.16 ± 0.05	6.3 ± 0.6	2.2 ± 0.1	20.16 ± 0.05	5.8 ± 0.4	223.6 ± 109.6	40.0	4_4
K16	10.1389	−72.7400	21.81 ± 0.07	12.5 ± 5.4	5.2 ± 3.2	21.81 ± 0.08	9.5 ± 2.3	26.8 ± 7.0	16.0	4_4
K17	10.2544	−72.5728	19.54 ± 0.07	7.7 ± 0.8	2.6 ± 0.1	19.50 ± 0.08	6.1 ± 0.5	169.4 ± 39.7	64.0	4_4
K21	10.3532	−72.8890	21.77 ± 0.08	27.3 ± 6.9	2.0 ± 0.4	21.81 ± 0.09	35.5 ± 6.5	292.0 ± 138.4	127.0	4_4
K25	12.0063	−73.4861	20.20 ± 0.22	6.0 ± 2.9	2.0 ± 0.7	20.35 ± 0.25	9.1 ± 3.6	59.4 ± 40.2	32.0	3_4
K27	12.0579	−73.8614	21.16 ± 0.08	12.0 ± 2.5	2.0 ± 0.3	21.27 ± 0.12	17.0 ± 3.5	132.5 ± 59.1	64.0	3_4
K28	12.9233	−71.9998	20.97 ± 0.05	20.1 ± 2.5	2.6 ± 0.3	20.96 ± 0.05	17.2 ± 1.4	272.6 ± 100.6	80.0	4_5
K30	13.1499	−72.1920	21.43 ± 0.14	21.9 ± 9.7	2.0 ± 0.7	21.51 ± 0.15	32.9 ± 10.7	176.5 ± 92.7	100.0	4_5
K31	13.2541	−72.8978	21.56 ± 0.09	43.7 ± 21.1	2.0 ± 1.0	21.61 ± 0.10	68.5 ± 26.8	230.5 ± 130.3	127.0	4_5
K34	13.8875	−72.8330	19.38 ± 0.04	16.9 ± 2.4	5.1 ± 0.9	19.36 ± 0.04	11.1 ± 0.8	47.5 ± 3.3	32.0	4_5
K38	14.4478	−73.4204	22.36 ± 0.10	41.6 ± 20.5	2.0 ± 1.0	22.42 ± 0.10	65.0 ± 24.5	228.3 ± 124.9	127.0	3_5
K4	5.7610	−73.6702	22.56 ± 0.07	14.6 ± 3.1	2.1 ± 0.3	22.60 ± 0.07	17.6 ± 2.5	181.8 ± 88.3	64.0	3_3
K42	15.1420	−72.3658	17.75 ± 0.13	2.6 ± 0.4	2.3 ± 0.2	17.73 ± 0.13	2.4 ± 0.3	80.4 ± 37.0	20.0	4_6
K43	15.2033	−73.3491	20.73 ± 0.12	7.8 ± 2.2	2.0 ± 0.4	20.87 ± 0.16	11.6 ± 3.1	76.5 ± 35.6	40.0	3_5
K44	15.5264	−73.9253	22.73 ± 0.09	52.7 ± 20.3	3.3 ± 1.4	22.73 ± 0.09	43.8 ± 10.5	254.2 ± 127.1	127.0	3_6
K45w	15.6973	−73.7384	20.63 ± 0.17	8.3 ± 3.3	4.1 ± 1.7	20.68 ± 0.15	7.4 ± 1.7	26.4 ± 4.0	20.0	3_6
K47	15.7982	−72.2721	18.88 ± 0.13	9.6 ± 2.5	4.6 ± 1.2	18.86 ± 0.16	6.0 ± 1.2	36.2 ± 6.4	25.0	4_6
K5	6.1770	−73.7546	20.85 ± 0.06	14.2 ± 1.8	2.6 ± 0.3	20.84 ± 0.06	12.3 ± 1.0	187.6 ± 55.1	64.0	3_3
K50	16.1512	−72.1611	19.73 ± 0.08	11.2 ± 4.8	3.1 ± 1.6	19.75 ± 0.08	11.3 ± 3.2	41.1 ± 19.4	20.0	4_6
K53	16.5568	−73.2973	20.62 ± 0.23	7.5 ± 4.6	2.0 ± 1.0	20.90 ± 0.07	27.5 ± 7.0	33.9 ± 1.6	32.0	3_6
K54	16.6988	−72.2725	19.67 ± 0.16	17.0 ± 6.2	5.1 ± 2.0	19.65 ± 0.19	10.2 ± 2.5	56.1 ± 12.7	40.0	4_6
K55	16.8846	−73.1217	20.89 ± 0.16	8.9 ± 2.8	2.3 ± 0.5	20.93 ± 0.17	9.6 ± 2.1	110.9 ± 55.1	50.0	3_6
K56	16.8670	−72.4927	20.61 ± 0.14	7.3 ± 2.5	2.1 ± 0.5	20.70 ± 0.13	10.3 ± 2.4	61.9 ± 24.4	32.0	4_6

Table C1 – *continued*

ID	RA (J2000)	Dec. (J2000)	EFF μ_0 (mag arcsec^{-2})	EFF α (arcsec)	EFF γ	King μ_0 (mag arcsec^{-2})	King r_c (arcsec)	King r_t (arcsec)	r_f (arcsec)	Tile
K57	17.0552	– 73.2583	21.41 ± 0.14	8.0 ± 4.7	2.0 ± 1.2	21.54 ± 0.12	13.8 ± 7.0	39.5 ± 27.7	20.0	3_6
K61	17.2663	– 73.0870	20.86 ± 0.18	6.5 ± 3.2	2.0 ± 0.8	21.14 ± 0.12	16.6 ± 7.0	33.2 ± 8.4	25.0	3_6
K63	17.6987	– 72.7935	20.39 ± 0.21	5.1 ± 2.2	2.0 ± 0.6	20.56 ± 0.20	8.0 ± 2.6	45.1 ± 21.1	25.0	4_6
K8	7.0067	– 73.3039	21.97 ± 0.11	8.1 ± 2.2	2.0 ± 0.4	22.08 ± 0.13	11.3 ± 2.6	86.3 ± 42.7	40.0	3_3
K9	7.5033	– 73.3790	22.44 ± 0.19	9.6 ± 4.6	2.0 ± 0.7	22.80 ± 0.13	20.6 ± 6.9	91.7 ± 48.6	50.0	3_3
L14	8.1683	– 72.5803	22.43 ± 0.13	10.2 ± 3.5	2.3 ± 0.6	22.48 ± 0.13	12.3 ± 3.0	78.9 ± 35.4	40.0	4_4
L19	9.4240	– 73.9055	22.72 ± 0.20	14.8 ± 13.7	2.0 ± 1.9	–	–	–	40.0	3_4
L28	10.7481	– 72.5890	19.35 ± 0.12	5.4 ± 0.8	2.7 ± 0.2	19.32 ± 0.10	4.4 ± 0.4	73.3 ± 11.1	40.0	4_4
L31	11.6503	– 72.7419	20.37 ± 0.08	5.7 ± 0.8	2.2 ± 0.2	20.38 ± 0.08	5.6 ± 0.5	124.3 ± 59.1	32.0	4_5
L33	11.8541	– 72.8415	20.19 ± 0.17	6.5 ± 2.0	2.6 ± 0.6	20.21 ± 0.18	6.3 ± 1.4	64.7 ± 27.5	32.0	4_5
L48	13.3672	– 71.3989	18.90 ± 0.14	9.6 ± 1.8	5.0 ± 0.8	18.85 ± 0.18	5.2 ± 0.8	38.7 ± 3.6	32.0	5_5
L51	13.7271	– 72.1141	18.92 ± 0.17	4.8 ± 1.5	2.2 ± 0.5	18.99 ± 0.17	5.5 ± 1.2	56.3 ± 27.7	26.0	4_5
L52	13.8220	– 73.5071	19.38 ± 0.07	4.6 ± 0.6	2.7 ± 0.2	19.35 ± 0.08	3.7 ± 0.3	54.3 ± 14.1	20.0	3_5
L56	14.3753	– 72.2648	16.58 ± 0.11	5.7 ± 0.7	3.9 ± 0.3	16.46 ± 0.20	3.2 ± 0.5	41.6 ± 4.1	32.0	4_5
L65	15.2521	– 72.7498	20.65 ± 0.31	6.7 ± 4.3	2.0 ± 0.8	21.11 ± 0.28	15.2 ± 9.2	72.4 ± 66.7	40.0	4_6
L66	15.4374	– 72.5643	17.31 ± 0.12	7.1 ± 1.4	4.7 ± 0.9	17.24 ± 0.11	4.3 ± 0.5	26.3 ± 2.0	20.0	4_6
L80	16.8675	– 72.7694	20.87 ± 0.11	10.6 ± 3.1	2.0 ± 0.4	20.97 ± 0.13	15.5 ± 3.6	94.0 ± 37.3	50.0	4_6
L91	18.2130	– 73.1198	21.89 ± 0.09	15.1 ± 6.3	2.8 ± 1.3	21.92 ± 0.09	17.2 ± 5.1	57.1 ± 22.5	32.0	3_6
L93	18.2029	– 73.4744	22.12 ± 0.06	15.5 ± 3.7	3.3 ± 0.9	22.11 ± 0.06	12.6 ± 1.8	77.6 ± 28.6	32.0	3_6
NGC 152	8.2329	– 73.1159	21.20 ± 0.07	24.4 ± 4.4	2.5 ± 0.4	21.20 ± 0.07	22.1 ± 2.6	320.0 ± 157.9	100.0	3_3
NGC 176	8.9929	– 73.1659	20.18 ± 0.11	16.4 ± 4.9	4.1 ± 1.3	20.17 ± 0.12	11.4 ± 2.2	67.9 ± 18.5	40.0	3_4
NGC 220	10.1280	– 73.4027	19.53 ± 0.09	11.4 ± 2.0	2.5 ± 0.3	19.52 ± 0.10	9.7 ± 1.2	200.0 ± 96.4	70.0	3_4
NGC 222	10.1838	– 73.3839	19.54 ± 0.17	8.0 ± 2.5	2.0 ± 0.4	19.62 ± 0.17	10.5 ± 2.2	132.2 ± 60.7	70.0	3_4
NGC 231	10.2770	– 73.3514	20.08 ± 0.16	9.4 ± 2.9	2.0 ± 0.4	20.25 ± 0.20	14.0 ± 3.6	152.9 ± 74.0	80.0	3_4
NGC 241	10.8827	– 73.4397	19.22 ± 0.16	7.4 ± 1.9	2.7 ± 0.5	19.19 ± 0.16	6.0 ± 1.1	91.8 ± 38.7	40.0	3_4
NGC 242	10.9026	– 73.4436	19.10 ± 0.19	4.6 ± 1.3	2.0 ± 0.3	19.27 ± 0.19	6.3 ± 1.3	86.7 ± 39.6	40.0	3_4
NGC 256	11.4753	– 73.5069	18.49 ± 0.11	14.1 ± 4.7	8.3 ± 3.7	18.57 ± 0.09	9.9 ± 1.4	21.9 ± 0.9	20.0	3_4
NGC 265	11.7984	– 73.4775	19.22 ± 0.06	12.8 ± 1.7	3.2 ± 0.4	19.20 ± 0.07	9.8 ± 0.9	96.7 ± 17.4	50.0	3_4
NGC 269	12.0892	– 73.5303	19.09 ± 0.04	7.0 ± 0.5	2.6 ± 0.1	19.07 ± 0.04	5.9 ± 0.3	119.4 ± 20.5	40.0	3_5
NGC 290	12.8113	– 73.1615	17.27 ± 0.22	2.3 ± 0.6	2.0 ± 0.2	17.49 ± 0.25	3.1 ± 0.7	77.7 ± 37.6	32.0	3_5
NGC 294	13.2736	– 73.3803	18.74 ± 0.03	11.4 ± 0.7	3.8 ± 0.2	18.71 ± 0.05	7.8 ± 0.4	62.3 ± 4.0	40.0	3_5
NGC 299	13.3533	– 72.1970	17.12 ± 0.12	6.5 ± 1.4	4.0 ± 0.8	17.06 ± 0.12	4.4 ± 0.6	30.7 ± 4.0	20.0	4_5
NGC 306	13.5617	– 72.2418	18.62 ± 0.17	8.3 ± 3.5	3.7 ± 1.7	18.75 ± 0.13	9.6 ± 2.3	24.7 ± 3.0	20.0	4_5
NGC 330	14.0764	– 72.4636	17.10 ± 0.10	13.3 ± 1.9	2.9 ± 0.3	17.07 ± 0.12	9.8 ± 1.1	185.6 ± 37.4	100.0	4_5
NGC 361	15.5451	– 71.6060	20.38 ± 0.05	19.2 ± 2.2	2.7 ± 0.3	20.38 ± 0.04	16.6 ± 1.1	196.7 ± 38.4	80.0	5_6
NGC 376	15.9732	– 72.8260	17.88 ± 0.19	12.5 ± 3.5	4.0 ± 0.9	17.85 ± 0.22	7.9 ± 1.7	69.5 ± 13.0	50.0	4_6
NGC 416	16.9963	– 72.3552	18.57 ± 0.09	9.2 ± 1.3	2.4 ± 0.2	18.54 ± 0.10	7.6 ± 0.8	286.0 ± 136.7	80.0	4_6
NGC 419	17.0730	– 72.8844	18.16 ± 0.04	15.1 ± 0.9	2.8 ± 0.1	18.11 ± 0.06	10.9 ± 0.6	240.3 ± 25.0	127.0	4_6
OGLE 132	15.5551	– 72.9679	–	–	–	21.29 ± 0.25	8.2 ± 6.2	20.8 ± 15.1	12.0	3_6
OGLE 172	10.4508	– 73.3919	20.87 ± 0.35	3.3 ± 2.4	5.3 ± 4.7	21.22 ± 0.08	5.5 ± 1.5	5.5 ± 0.2	5.0	3_4
OGLE 28	11.3667	– 72.8199	20.80 ± 0.30	1.9 ± 0.9	2.0 ± 0.6	21.19 ± 0.29	3.7 ± 1.9	13.6 ± 8.0	8.0	4_4
OGLE 5	9.8419	– 73.2580	22.16 ± 0.22	3.1 ± 2.0	4.2 ± 3.1	22.38 ± 0.09	5.5 ± 2.0	6.0 ± 0.5	5.0	3_4
OGLE 53	12.3182	– 73.2116	20.33 ± 0.17	3.0 ± 2.1	2.0 ± 1.5	20.56 ± 0.08	8.0 ± 6.0	10.2 ± 3.9	6.0	3_5
OGLE 6	9.8885	– 73.1815	19.62 ± 0.65	0.6 ± 0.3	2.0 ± 0.2	20.34 ± 0.42	1.1 ± 0.4	14.3 ± 6.2	6.0	3_4
RZ 140	15.6803	– 71.4808	22.04 ± 0.27	4.1 ± 2.2	2.0 ± 0.7	22.23 ± 0.26	6.5 ± 2.5	36.3 ± 20.3	20.0	5_6
RZ 82	13.2911	– 71.9957	21.75 ± 0.12	4.3 ± 1.2	2.6 ± 0.7	21.80 ± 0.12	4.4 ± 0.9	26.7 ± 10.0	12.0	4_5

APPENDIX D: PROFILES – FIGURE

In Fig. D1 (online supplementary material), we display all SBPs with the best fit obtained through the EFF (red line) and King (blue line) profiles.

This paper has been typeset from a TEX/LATEX file prepared by the author.